Research Article
DILI, Autoimmune, Cholestatic and Genetic Diseases

JOURNAL
OF HEPATOLOGY

Morphologic and molecular analysis of liver injury after SARS-CoV-2 vaccination reveals distinct characteristics

Sarp Uzun[1], Carl P. Zinner[1], Amke C. Beenen[1], Ilaria Alborelli[1], Ewelina M. Bartoszek[2], Jason Yeung[3], Byron Calgua[1], Matthias Reinscheid[4,5], Peter Bronsert[6,7], Anna K. Stalder[1], Jasmin D. Haslbauer[1], Juerg Vosbeck[1], Luca Mazzucchelli[8], Tobias Hoffmann[9], Luigi M. Terracciano[10,11], Gregor Hutter[12,13], Michael Manz[14], Isabelle Panne[14], Tobias Boettler[4], Maike Hofmann[4], Bertram Bengsch[4,15,16], Markus H. Heim[14,17], Christine Bernsmeier[14,17], Sizun Jiang[3,18,19], Alexandar Tzankov[1], Benedetta Terziroli Beretta-Piccoli[20,21,22], Matthias S. Matter[1,*]

Journal of Hepatology **2023**. vol. 79 | 666–676

Background & Aims: Liver injury after COVID-19 vaccination is very rare and shows clinical and histomorphological similarities with autoimmune hepatitis (AIH). Little is known about the pathophysiology of COVID-19 vaccine-induced liver injury (VILI) and its relationship to AIH. Therefore, we compared VILI with AIH.
Methods: Formalin-fixed and paraffin-embedded liver biopsy samples from patients with VILI (n = 6) and from patients with an initial diagnosis of AIH (n = 9) were included. Both cohorts were compared by histomorphological evaluation, whole-transcriptome and spatial transcriptome sequencing, multiplex immunofluorescence, and immune repertoire sequencing.
Results: Histomorphology was similar in both cohorts but showed more pronounced centrilobular necrosis in VILI. Gene expression profiling showed that mitochondrial metabolism and oxidative stress-related pathways were more and interferon response pathways were less enriched in VILI. Multiplex analysis revealed that inflammation in VILI was dominated by $CD8^+$ effector T cells, similar to drug-induced autoimmune-like hepatitis. In contrast, AIH showed a dominance of $CD4^+$ effector T cells and $CD79a^+$ B and plasma cells. T-cell receptor (TCR) and B-cell receptor sequencing showed that T and B cell clones were more dominant in VILI than in AIH. In addition, many T cell clones detected in the liver were also found in the blood. Interestingly, analysis of TCR beta chain and Ig heavy chain variable-joining gene usage further showed that TRBV6-1, TRBV5-1, TRBV7-6, and IgHV1-24 genes are used differently in VILI than in AIH.
Conclusions: Our analyses support that SARS-CoV-2 VILI is related to AIH but also shows distinct differences from AIH in histomorphology, pathway activation, cellular immune infiltrates, and TCR usage. Therefore, VILI may be a separate entity, which is distinct from AIH and more closely related to drug-induced autoimmune-like hepatitis.

Introduction

Severe acute respiratory syndrome coronavirus 2 (SARS-CoV-2), the causative agent of coronavirus disease 2019 (COVID-19), has infected millions of people worldwide with a great socio-economic impact.[1] The most effective strategy to reduce morbidity and mortality from SARS-CoV-2 infection is the development of safe and effective vaccines. Several different COVID-19 vaccines have been approved and millions of people have received a dose to date.[2] Since the introduction of COVID-19 vaccines, potential adverse events have been reported. Most of them are mild and include local symptoms, fatigue, fever, headache, and myalgia.[2] Rarely, COVID-19 vaccination has been associated with autoimmune disorders such as myocarditis, immune thrombocytic thrombocytopaenia, and Guillain-Barré syndrome.[2] In addition, several recent reports have described hepatitis following COVID-19 vaccination as a very rare event and supported a direct correlation.[3–11] Multiple potential mechanisms of COVID-19 vaccine-related tissue injury have been suggested, including molecular mimicry, triggering of a latent autoimmune disease, vaccine-induced specific antibody production, bystander activation with polyclonal B cell expansion, epitope spreading, and the effects of particular adjuvants.[2,12–14]

COVID-19 vaccine-induced liver injury (VILI) resembles autoimmune hepatitis (AIH) clinically, biochemically, morphologically and, to some extent, also serologically.[10,11,15] Many, but not all, patients with VILI fulfil the criteria for the diagnosis of AIH.[10,11,16,17] However, it is not known whether hepatitis following COVID-19 vaccination is a form of triggered AIH or

Keywords: Autoimmune hepatitis; COVID-19; Drug-induced liver injury; SARS-CoV-2; Vaccination.
Received 17 August 2022; received in revised form 10 May 2023; accepted 19 May 2023; available online 7 June 2023
* Corresponding author. Address: Institute of Pathology, University Hospital Basel, Basel, Schoenbeinstrasse 40, CH-4031 Basel, Switzerland. Tel.: +41 61 328 64 71.
E-mail address: matthias.matter@usb.ch (M.S. Matter).
https://doi.org/10.1016/j.jhep.2023.05.020

whether it rather belongs to a condition described as drug-induced autoimmune-like hepatitis (DI-AILH).[18,19] Furthermore, very little is known about the pathophysiology of this phenomenon.[20]

In this study, we aimed to characterise the morphological and molecular features of VILI and compare them with those of patients with AIH. By using gene expression profiling, immune repertoire sequencing, and multiplex immunofluorescence we show that both entities share some features but also have distinct differences.

Materials and methods

The materials and methods can be found in the supplementary documents online.

Ethical statement

The study was approved by the ethics commission of Northern Switzerland (EKNZ; study ID: 2020-00969), the ethics commission at the Albert-Ludwigs-University, Germany and the Comitato Etico cantonale Ticino, Switzerland. All tissue samples were collected as part of the routine diagnostic workup and selected retrospectively, informed consent was obtained from all vaccinated patients, and the study was conducted according to the Declaration of Helsinki (1975).

Results

Characteristics of study and control cohort

In our study, we included formalin-fixed and paraffin-embedded (FFPE) liver biopsies from six patients with COVID-19 VILI (Table 1, Tables S1, and S2). All patients received mRNA-1273 from Moderna, the vaccine most commonly administered in Switzerland. Two patients have been described in previous publications.[6,11] Average patient age was 58 (range 21–85 years). Two patients were female and four were male. Three patients developed symptoms after the first vaccination and three after the second. The main symptoms were fatigue, jaundice, and nausea. The time to symptom onset varied from 2 to 28 days after vaccination. Patients did not have autoimmune diseases, except for one patient (VILI3), who had a history of elevated antibodies against thyroid peroxidase and polymyalgia. All patients were negative by PCR or antibody testing for viral hepatitis (hepatitis A, B, C, D, and E) and none of the patients had a history of clinically apparent COVID-19 disease. At the time of vaccination, two patients were taking several medications for concomitant diseases for more than 5 years (VILI5: aspirin, rosuvastatin, metformin; VILI6: lercanidipine, telmisartan). One patient had been taking oral contraceptives for 3 years and took herbal medicines for a short time a few months before vaccination. One patient regularly took multivitamin supplements. The remaining two patients have not taken any medicine. None of the patients had any prior history of liver disease or alcohol abuse. After the liver biopsy, five patients received prednisone. One patient did not receive any treatment. All patients improved and remained in remission during the follow-up period (Table 1).

Because VILI resembles AIH,[10,11] we selected archived FFPE liver biopsies from untreated patients with Type 1 AIH (n = 9) for comparison, which were taken at the time of initial diagnosis of AIH and early after appearance of symptoms (Tables S1 and S2). Patients with AIH were on average 61 years old (range 49–78 years) and were predominantly female (n = 8).

Clinical and histological comparison

Serum liver enzyme levels (aspartate aminotransferase [AST], alanine aminotransferase [ALT], gamma-glutamyl transferase [GGT], alkaline phosphatase [ALP], and bilirubin) were increased in both cohorts. In comparison with patients with AIH, VILI showed higher levels of AST, ALT, and bilirubin, but lower levels of GGT and ALP, without reaching statistical significance (Tables S1 and S2). Liver injury calculated with the R ratio[21] was hepatocellular in all patients with VILI and AIH, except for one patient with AIH, who had mixed, hepatocellular, and cholestatic liver injury. Serum autoantibodies in the VILI cohort showed anti-nuclear antibodies (ANAs) in three cases, of whom one additionally showed atypical anti-mitochondrial antibodies (AMAs); one patient showed elevated anti-actin antibodies (AAAs) only (Tables S1 and S2). Therefore, four out of six (67%) patients with VILI were ANA or AAA positive. In the AIH cohort, seven patients were ANA positive, two of them in conjunction with elevated anti-smooth muscle antibodies (ASMA) or AAA. Two additional patients had either elevated ASMA or AAA only. Therefore, all patients from the AIH cohort showed elevated ANA and/or elevated ASMA/AAA. Anti-soluble liver antigen (anti-SLA), anti-liver-kidney microsome 1 (anti-LKM1), and anti-liver cytosol type 1 (anti-LC1) were negative in all patients from both cohorts. Two patients with AIH also showed anti-neutrophil cytoplasmic antibodies (ANCAs). IgG levels were increased in two out of the five tested patients with VILI, and in four out of eight tested patients with AIH.

After the appearance of symptoms, all patients underwent liver biopsy (2-90 days after symptoms for VILI and 9-150 days for AIH) and histological analysis according to current recommendations.[22–24] Variable degrees of piecemeal necrosis, focal

Table 1. Cohort of patients with liver injury after COVID-19 vaccination.

Patient ID	Age	Sex	Symptoms	Symptoms after vaccination	Drugs at time of vaccination	Therapy (prednisone)*	Follow-up (months)	Remission
VILI1	48	F	Fatigue, abdominal pain	2 days after 2nd vaccination	Multivitamins	40 mg/d for 3 months	18	Yes
VILI2	85	M	Nausea, dark urine	5 days after 1st vaccination	None	None	18	Yes
VILI3	21	F	Fatigue, jaundice, nausea	21 days after 2nd vaccination	Oral contraceptive	60 mg/d for 3 months	15	Yes
VILI4	53	M	Fatigue, jaundice, nausea	7 days after 2nd vaccination	None	40 mg/d for 3 months	18	Yes
VILI5	63	M	Fatigue, jaundice, weight loss	10 days after 1st vaccination	Aspirin, rosuvastatin, metformin	40 mg/d for 11 months	18	Yes
VILI6	78	M	None	28 days after 1st vaccination†	Lercanidipine, telmisartan	40 mg/d for 5 months	12	Yes

*Initial dose, reduced thereafter according to liver enzyme levels and/or clinical course.
†Only elevated liver enzymes.

lytic necrosis/apoptosis/inflammation, and portal inflammation were found without significant differences between the two cohorts (Tables S1, S3, and Fig. S1). In contrast, confluent necrosis was more extensive in VILI (p = 0.0025). The summarised Ishak grading score[24] was similar in both cohorts and between 3 and 16 (average 12.2) in patients with VILI and 6 to 14 (average 10.3) in patients with AIH. In all patients with VILI and five patients with AIH no fibrosis was found, corresponding to Ishak stage 0. Four patients with AIH presented with stage 1 fibrosis. Rosette formation, emperipolesis, endothelialitis, and cholestasis were frequently found in both cohorts.[22,23] Bile duct injury was present in only one patient of the VILI cohort and two patients of the AIH cohort. None of the patients showed steatosis. Likewise, there was no difference in the number of eosinophils between both cohorts.

In summary, histological analysis revealed a diagnosis of likely AIH in five out of six patients with VILI and a diagnosis of possible AIH in one patient according to the most recent recommendations.[23] Moreover, three out of five patients with VILI had a probable/definite AIH score according to the simplified AIH criteria (Table S1).[17] For one patient with VILI, not all values were available for calculation. In contrast, all patients with AIH showed histologically the diagnosis of a likely AIH and a probable/definite AIH score according to the simplified criteria.

Patients with VILI and AIH have related but clearly different gene expression profiles

To understand the different biological mechanisms between VILI and AIH, we performed whole transcriptome profiling with bulk RNA, isolated from FFPE liver biopsies of patients with VILI and AIH. As further controls, we added liver biopsies from patients with alcoholic steatohepatitis (ASH; n = 17) and chronic HCV infection (n = 13). Patients with HCV were untreated and showed high viral load at the time of biopsy. The average patient age was 64.3 years for ASH and 58.3 years for HCV, and both cohorts had cirrhotic liver disease (Table S4). Additionally, we included three patients with histologically normal liver tissue, who presented with a metastasis to the liver (two with pancreatic and one with urothelial carcinoma) (Table S4).

Principal component analysis showed that patients with VILI and AIH had different transcriptome profiles but were close to each other and significantly different from patients with chronic HCV infection or ASH (Fig. 1A). Two patients with VILI (#1 and #2) and one patient with AIH (#7) clustered close to normal liver samples. Interestingly, all of these three patients had little inflammation signature according to RNA transcriptome (see Fig. 2A below). Differential gene expression analysis revealed 70 genes (43 upregulated and 27 downregulated) that showed a significant difference between the VILI and AIH cohort (log fold change [lfc] >0.58, p_{adj} <0.05) (Fig. 1B and Table S5). To validate our gene expression profiling data, we selected one significantly upregulated and one significantly downregulated gene and performed a qPCR. As an upregulated gene we selected *TSPAN8* (lfc = 2.172, p_{adj} = 0.002), which has been shown to correlate with SARS-CoV-2 infection rate,[25] and *RNF213* (lfc = -0.793, p_{adj} = 0.026), associated with immune response and interferon signalling.[26] Expression changes were confirmed by qPCR for both genes (Fig. 1C). Unsupervised hierarchical clustering of VILI and AIH samples based on the differentially expressed genes further showed that samples belonging to the same cohort clustered together (Fig. 1D). Finally, we performed gene set enrichment analysis (GSEA) to identify biological processes characteristic of the VILI and AIH cohort (Fig. 1E and Table S6). We found that pathways related to immune response were overrepresented in the AIH cohort, in particular gene sets associated with interferon response (*e.g.* Hallmark Interferon-Gamma Response, Reactome Interferon Gamma Signalling, and Hallmark Interferon Alpha Response). In contrast, mitochondrial metabolism and oxidative stress-related pathways were overrepresented in the VILI cohort. Because we performed transcriptome analysis from bulk RNA, we could not determine the cell type responsible for the observed differences. However, it is known that drug-induced liver injury (DILI) results from mitochondrial toxicity and impairment of the oxidation–phosphorylation machinery in hepatocytes.[27,28] Therefore, we carried out spatial whole transcriptome analysis with the GeoMx platform (Nanostring, Seattle, USA) selecting arginase positive hepatocytes from periportal and centrilobular regions of VILI and AIH (Fig. S2A and B). We found 53 genes (38 upregulated and 15 downregulated) demonstrating a significant differential expression between the two cohorts (lfc >0.58, p_{adj} <0.05) (Fig. S2C and Table S7). GSEA revealed that the same four oxidative phosphorylation or liver metabolism related gene sets, which were enriched in bulk-RNA sequencing, were also significantly enriched with the spatial transcriptomic analysis of hepatocytes (Fig. S2D and Table S8). Therefore, hepatocytes are the main cells responsible for the differences between both cohorts in mitochondrial toxicity and impairment of the oxidation–phosphorylation machinery.

In summary, our data suggest that although VILI and AIH are related based on their expression profiles, they have distinct differences in biological processes.

Immunoprofiling shows higher portal/periportal CD8$^+$ T cell infiltration but lower B cell infiltration in VILI

Next, we characterised the immune infiltrates in the biopsy tissue. First, we performed a cell type enrichment analysis with our RNA gene expression data by using the xCell web tool.[29] Interestingly, we observed a more enriched 'B cells' signature in patients with AIH in comparison with patients with VILI (p = 0.0048); however, it did not reach significance after adjustment to multiple testing (p_{adj} = 0.1150) (Fig. 2A). In contrast to B cells, no enrichment difference was observed between the two cohorts for the other immune cell signatures.

Thereafter, we carried out multiplex immunofluorescence with co-detection by indEXing (CODEX; Akoya Biosciences, Marlborough, USA)[30] on FFPE liver biopsies of our cohorts with sufficient remaining tissue, resulting in the analysis of five patients with VILI and seven patients with AIH. By using different immune markers simultaneously (Fig. S3A), we assessed the density and differential localisation of B and T cells within the portal and centrilobular region of the liver parenchyma (Fig. 2B and Fig. S3B). CD79a was used as a marker for B cells including plasma cells, CD20 for B cells, CD3, CD8, CD4, and FoxP3 for respective T effector and regulatory T cells. CD3-positive T cells showed overall the highest cell density and were slightly more prominent in the portal region than in the centrilobular region in both cohorts (Fig. 2C and Fig. S3C). CD3$^+$ CD8$^+$ T effector cells showed a trend for a higher density

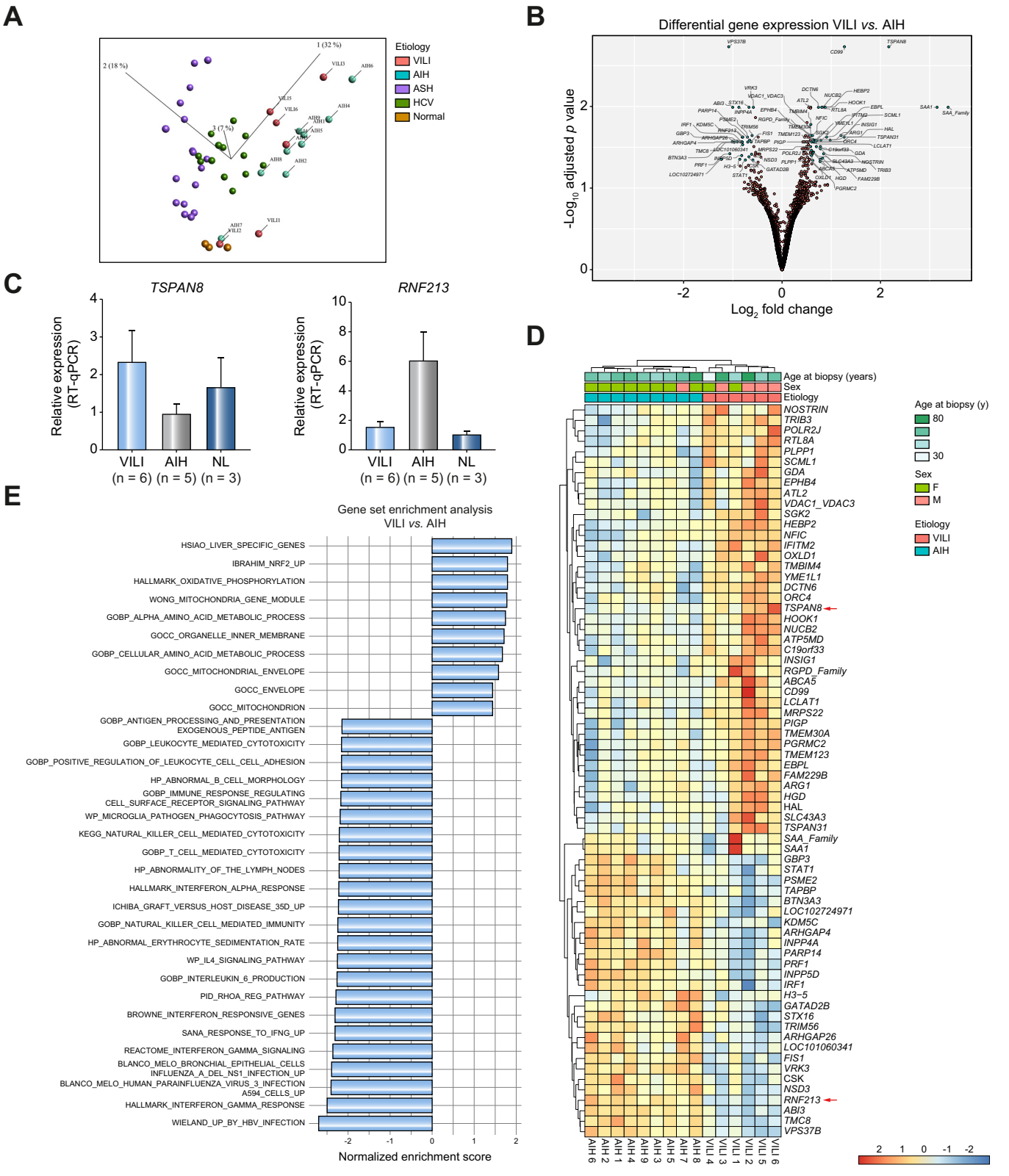

Fig. 1. Whole transcriptome analysis reveals distinct differences between VILI and AIH. (A) Principal component analysis of VILI (n = 6), AIH (n = 9), ASH (n = 17), HCV hepatitis (n = 13) and normal liver (n = 3). (B) Volcano plot for differentially expressed genes between VILI and AIH cohort. Genes with a $\log_2$ fold change >0.58 and p_{adj} <0.05 were accepted as differentially expressed between cohorts. (C) qPCR result of *TSPAN8* and *RNF213* expression. VILI cohort, n = 6; AIH cohort, n = 5; normal liver, n = 3. (D) Unsupervised hierarchical clustering with differentially expressed genes between VILI and AIH samples. Arrows show the two genes which underwent validation of gene expression by qPCR. (E) Gene set enrichment analysis of VILI and AIH cohorts. Only pathways with p_{adj} <0.05 are shown. AIH, autoimmune hepatitis; ASH, alcoholic steatohepatitis; VILI, vaccine-induced liver injury.

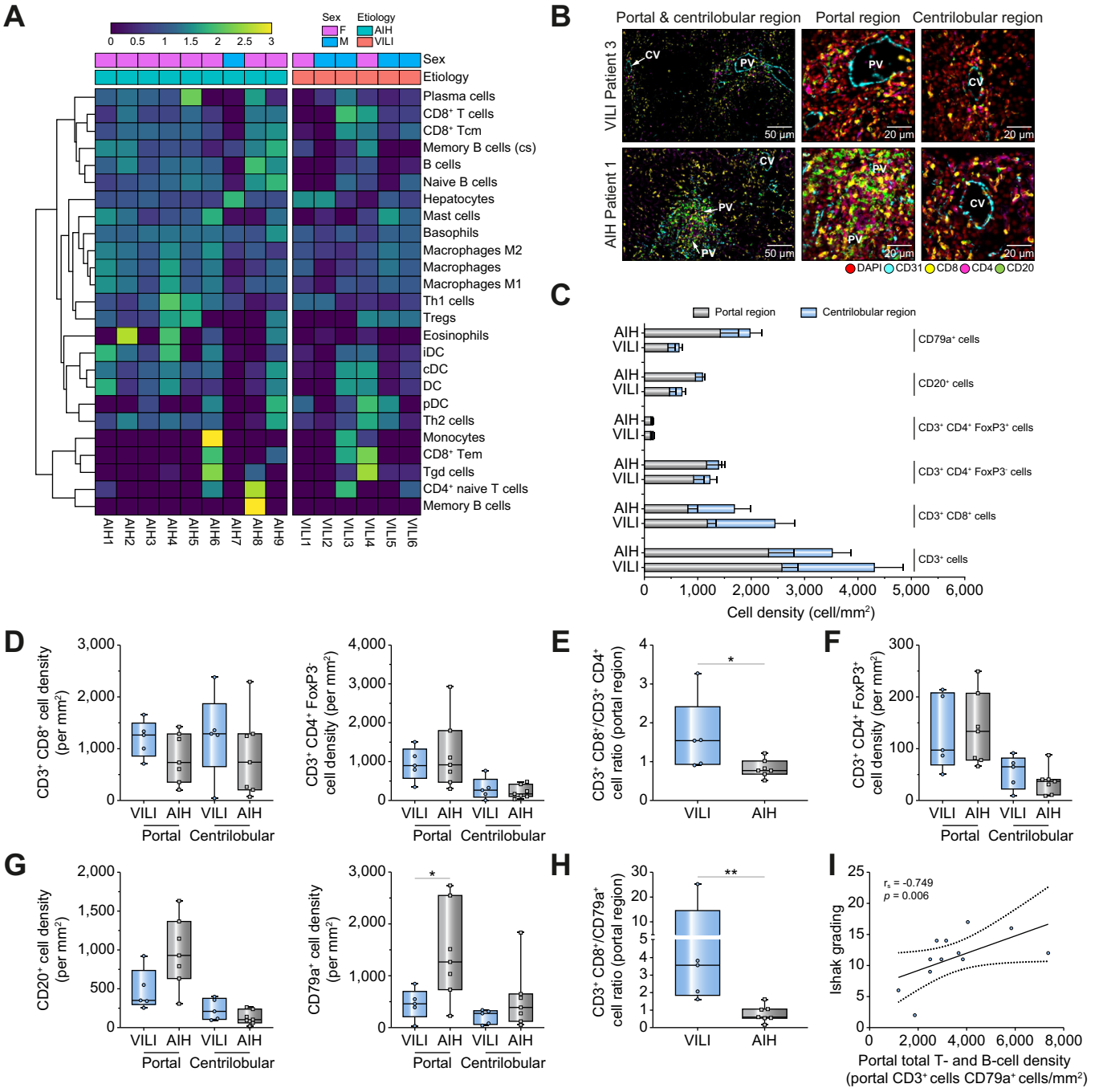

Fig. 2. Immunophenotyping of VILI and AIH with xCell method and multiplex immunofluorescence. (A) *In silico* immunophenotyping of VILI and AIH cases with xCell method. (B) Portal and centrilobular immune cell densities were quantified with CODEX multiplex immunofluorescence. (C) Immune cell distribution in the portal and centrilobular region of VILI and AIH samples. Bar graphs indicate mean and SEM of immune cell densities (cells/mm^2). (D) CD3$^+$ CD8$^+$ and CD3$^+$ CD4$^+$ FoxP3$^-$ cell density in the portal and centrilobular region of VILI and AIH samples. (E) Ratio of CD3$^+$ CD8$^+$/CD3$^+$ CD4$^+$ T cells in the portal region of VILI and AIH cohorts. (F) CD3$^+$ CD4$^+$ FoxP3$^+$ cell density in the portal and centrilobular region of VILI and AIH samples (G) CD20$^+$ and CD79a$^+$ cell density in the portal and centrilobular region of VILI and AIH samples. (H) Ratio of CD3$^+$ CD8$^+$/CD79a$^+$ T cells in the portal region of VILI and AIH cohorts. (I) Correlation analysis between Ishak grading and portal total T cell (CD3$^+$) and B cell (CD79a$^+$) density. The black line shows the linear regression line and dotted lines represent the 95% CI upper and lower limits. Each dot represents a patient. *p <0.05, **p <0.01 (two-group comparison: Wilcoxon rank-sum test, correlation analysis: Spearman rank correlation test). AIH, autoimmune hepatitis; CV, central vein; PV, portal vein; VILI, vaccine-induced liver injury.

in VILI than in AIH in the portal (1264 *vs.* 734 cells/mm^2) and centrilobular region (1288 *vs.* 739 cells/mm^2), which did not reach significance (Fig. 2D). CD3$^+$ CD4$^+$ FoxP3$^-$ T effector cell density was similar between VILI and AIH in the portal (897 *vs.* 917 cells/mm^2) and centrilobular region (265 *vs.* 170 cells/mm^2, Fig. 2D). Variability in immune cell density between patients within each cohort was high (Figs. S3C and S3D), which was already appreciated from the Ishak grading and whole transcriptome analysis described above. Therefore, we calculated the ratio between CD3$^+$ CD8$^+$ and CD3$^+$ CD4$^+$ effector T cells.

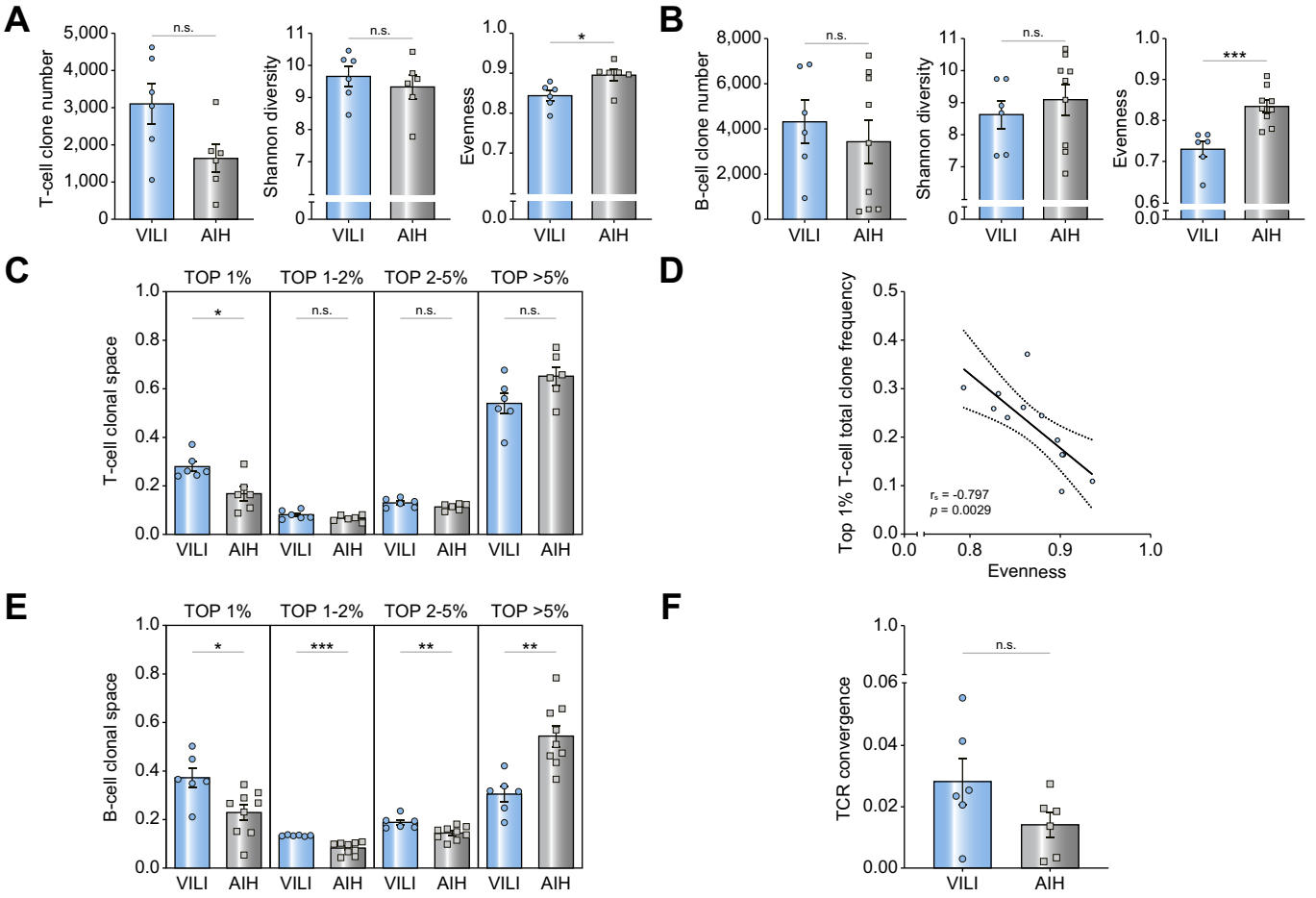

Fig. 3. Global immune metrics and clonal space analysis of TCR and BCR repertoires of VILI and AIH. (A) Global TCR repertoire metrics (clone number, Shannon diversity, evenness) of VILI (n = 6) and AIH (n = 6) patients. (B) Global BCR repertoire metrics (clone number, Shannon diversity, evenness) of VILI (n = 6) and AIH (n = 9) cohorts. (C) Clonal space occupied by T cell clones according to their frequency ranking. (D) Correlation of top 1% ranked total TCR frequency and evenness of VILI and AIH TCR repertoires. The black line shows the linear regression line and dotted lines represent the 95% CI upper and lower limits. (E) Clonal space occupied by B cell clones according to their frequency ranking. (F) TCR convergence of VILI and AIH cohorts. Each dot represents a patient. *p <0.05, **p <0.01, ***p <0.001 (two-group comparison: unpaired Student t test, correlation analysis: Spearman rank correlation test). AIH, autoimmune hepatitis; BCR, B-cell receptor; ns, not significant; TCR, T-cell receptor; VILI, vaccine-induced liver injury.

Interestingly, the proportion of $CD3^+$ $CD8^+$ effector T cells in patients with VILI was significantly higher than in patients with AIH (1.541 *vs.* 0.7706; p = 0.0303; Fig. 2E), indicating that the immune infiltrate in VILI was dominated by $CD3^+$ $CD8^+$ T cells.

Next, we analysed $CD3^+$ $CD4^+$ $FoxP3^+$ Treg cell distribution, which was similar in both cohorts (Fig. 2F). Finally, $CD20^+$ and $CD79a^+$ B cells both showed a lower density in VILI than in AIH in the portal region (CD20: 350.7 *vs.* 929.3 cells/mm^2; $CD79a^+$: 459.5 *vs.* 1267 cells/mm^2), which reached significance for $CD79a^+$ B cells (p = 0.0480) (Fig. 2G). In the centrilobular region, $CD20^+$ B cells were similar between both cohorts, but $CD79a^+$ B cells also showed a lower density in VILI than in AIH. Interestingly, we also observed a trend towards a positive correlation between portal $CD79a^+$ B cell density and serum IgG levels in VILI and AIH cases; however, it did not reach statistical significance (r_s = 0.639, p = 0.052) (Fig. S3E).

In conclusion, inflammation in VILI was dominated by $CD8^+$ effector T cells, whereas AIH showed a significantly higher portal infiltrate of $CD79a^+$ B cells and plasma cells. Indeed, the ratio of $CD3^+$ $CD8^+$ T effector cells to $CD79a^+$ B cells was significantly higher in VILI than in AIH (Fig. 2H). The total density of T and B cells also correlated with Ishak grading (r_s = 0.749, p = 0.006) which indicated that our histopathological observations are in line with multiplex immunofluorescence analysis (Fig. 2I). In addition, we compared a small cohort (n = 4) of DI-AILH with VILI and AIH. Liver histology, serology, and clinical characteristics of DI-AILH patients showed similarities with AIH (Tables S9 and S10). Two patients had a definite and two a probable AIH score according to the simplified AIH criteria.[17] Interestingly, the proportion of $CD3^+$ $CD8^+$ to $CD3^+$ $CD4^+$ effector T cells and $CD3^+$ $CD8^+$ to $CD79a^+$ B cells was higher in patients with DI-AILH than in patients with AIH (1.255 *vs.* 0.7706 and 6.316 *vs.* 0.6023) (Fig. S4), indicating that the composition of the immune infiltrate in DI-AILH is similar to VILI but different from AIH.

VILI cohort shows less evenness in TCR and BCR repertoire and larger clonal space of top 1% T cell clones

As a next step, we characterised the clonal distribution of the adaptive immune infiltrate in patients with VILI and AIH. We performed NGS-based immunoprofiling by sequencing the CDR3 region of the T-cell receptor (TCR) and B-cell receptor

(BCR) from bulk RNA isolated from liver biopsies. After applying stringent quality criteria, we obtained valid NGS data from all samples for BCR analysis (n = 15), whereas TCR analysis was carried out with six samples from each cohort (n = 12).

First, we started with the analysis of global immune repertoire metrics to assess clone number, diversity, and clonality as parameters for immunological complexity and for ongoing, successful, or deregulated immune response. Although VILI had increased T and B cell clone numbers, we did not find a significant difference between both cohorts (Fig. 3A and B). Moreover, the Shannon Diversity Index of both cohorts was similar in TCR and BCR repertoires. However, we found that VILI had significantly lower evenness in the TCR (p = 0.0212) and BCR repertoire (p = 0.0008), which indicated that VILI had more expanded clones in T and B cell architecture in comparison with AIH (Fig. 3A and B). Indeed, the spectratyping plots of T and B cell clone distribution in VILI samples showed few expanded T and B cell clones, suggesting a clonal expansion against specific antigens (Fig. S5A and B). In contrast, the clonal distribution of T and B cells was mainly composed of unexpanded clones in AIH samples, which suggested a more polyclonal reaction against antigenic stimulations (Fig. S5A and B). Next, we tested whether the evenness difference between the two cohorts arises specifically from the most abundant T and B cell clones in the liver tissues. For this purpose, we performed clonal space analysis that was previously used to determine which ranges of clones are associated with the TCR repertoire difference.[32,33] First, T and B cell clones were divided into four groups according to their ranked frequencies (top 1%, top 1–2%, top 2–5%, and >5%). Thereafter, the clone frequency in each group in relation to the total immune repertoire was calculated. As expected from the difference in evenness, we found that the T cell clones in the top 1% group of the VILI cohort had a significantly larger clonal space compared to the AIH cohort (27.9% *vs.* 16.8%; p = 0.0104; Fig. 3C). This suggests that this group of T cells is the main responder against vaccination-related antigenic stimulation. In contrast, there was no difference in the top 1–2% and top 2–5%. Since the T cell architecture was dominated by the top 1% in VILI samples, the >5% group occupied a larger space in AIH compared with the VILI cohort, however, it did not reach significance (mean VILI *vs.* AIH: 54.0% *vs.* 65.1%, p = 0.0754). We also tested whether the total frequency of top 1% T cell clones correlated with the evenness in each patient and found that these two parameters showed a significant inverse correlation with each other (r_s = -0.797, p = 0.0029; Fig. 3D). In the B cell compartment, the top 1%, top 1–2%, and top 2–5% had a significantly larger clonal space in the VILI cohort, whereas the >5% group occupied a larger space in AIH than in VILI (Fig. 3E). This highlights the more pronounced presence of a general B cell clone expansion in VILI samples and is consistent with the difference in evenness between VILI and AIH samples (Fig. 3E).

Next, we analysed in more detail the sharing of T cell clone sequences and their specificity. Of the 184 top 1% T cell clones from all six VILI liver samples, no shared clones were detected among them. Yet, when we uploaded the beta chain CDR3 sequences of the 184 top 1% liver T cell clones to a publicly available TCR database (http://tools.iedb.org/tcrmatch/), we found seven spike SARS-CoV-2 glycoprotein epitopes that matched with CDR3 sequences (Table S11), indicating that some high-frequency T cell clones may possibly recognise the spike glycoprotein. For one patient (VILI #5), a blood sample was available from the time of liver biopsy. Therefore, we searched for shared T cell clones between the blood sample and the liver biopsy. Interestingly, of the 47 top 1% T cell clones of the liver, we found 13 shared T cell clones within the blood sample (Table S12). To further determine whether shared clones could represent SARS-CoV-2 spike-protein specific T cells, we analysed an additional patient (VILI_F) recently published in a case report, who was found to have a $CD8^+$ T cell response against a pre-described Spike-protein epitope ($S_{378-386}$) of SARS-CoV-2.[9] However, the number of sorted $S_{378-386}$ tetramer-positive cells from PBMCs, which represent only a fraction of the whole anti-Spike T cell response, was insufficient for following TCR sequencing. However, we were able to perform TCR sequencing from the $S_{378-386}$-depleted fraction. Interestingly, all of the top 1% T cell clones (n = 10) and 96% (n = 47) of the top 50 most frequent T cell clones in the liver could be detected in PBMC-sorted spike-protein negative T cell clones (Table S13). Yet, none of the shared T cell clones between liver and blood of these two patients matched to the TCR database described above. Finally, we looked at TCR convergence which was suggested as an indicator of antigen-specific T cell response.[31] Although we observed a higher convergence in VILI samples, it did not reach significance (mean VILI *vs.* AIH: 2.8% *vs.* 1.4%; p = 0.1248; Fig. 3F).

In conclusion, our data indicate that COVID-19 vaccination leads to the expansion of a unique set of T cells in the liver, many of which can also be detected in the blood.

Immune repertoires of VILI and AIH samples have an identical CDR3 length distribution but show variations in TCR beta variable-joining and immunoglobulin heavy chain variable-joining gene usage

The diversity of CDR3 length is one of the critical determinants of the antigen recognition process by T and B cells. Therefore, we compared CDR3 length distribution in both cohorts. VILI and AIH showed a similar CDR3 length distribution pattern with comparable mean CDR3 nucleotide length in both TCR (36.72 *vs.* 36.42; Fig. 4A) and BCR (45.78 *vs.* 46.76; Fig. 4B) repertoires. We next evaluated the variable and joining (V-J) region usage in TCR and BCR repertoires of VILI and AIH samples. As shown in Fig. 4C, T and B cell clones from different patients of the same cohort had a distinct pattern of TCR beta variable-joining (TRBV-J) and immunoglobulin heavy chain variable-joining (IgHV-J) usage and each sample had a different set of V-J genes, which was overrepresented or underrepresented. Previously, it was reported that TRBV6-1 and TRBV6-4 were used less frequently in patients with AIH compared with normal controls.[32] Accordingly, we observed that TRBV6-1 and TRBV6-4 genes were used less frequently in the AIH cohort compared with the VILI cohort; however, only TRBV6-1 was statistically significant (Fig. 4D). Besides, TRBV5-1 was significantly less and TRBV7-6 was significantly more frequently used in VILI in comparison with the AIH cohort (Fig. 4D). Only one gene from the IgH repertoire, IGHV1-24, displayed a significant usage difference and was found less frequently in the VILI cohort (Fig. 4E).

Discussion

A growing body of evidence indicates a direct causality between COVID-19 vaccination and hepatitis in very rare cases

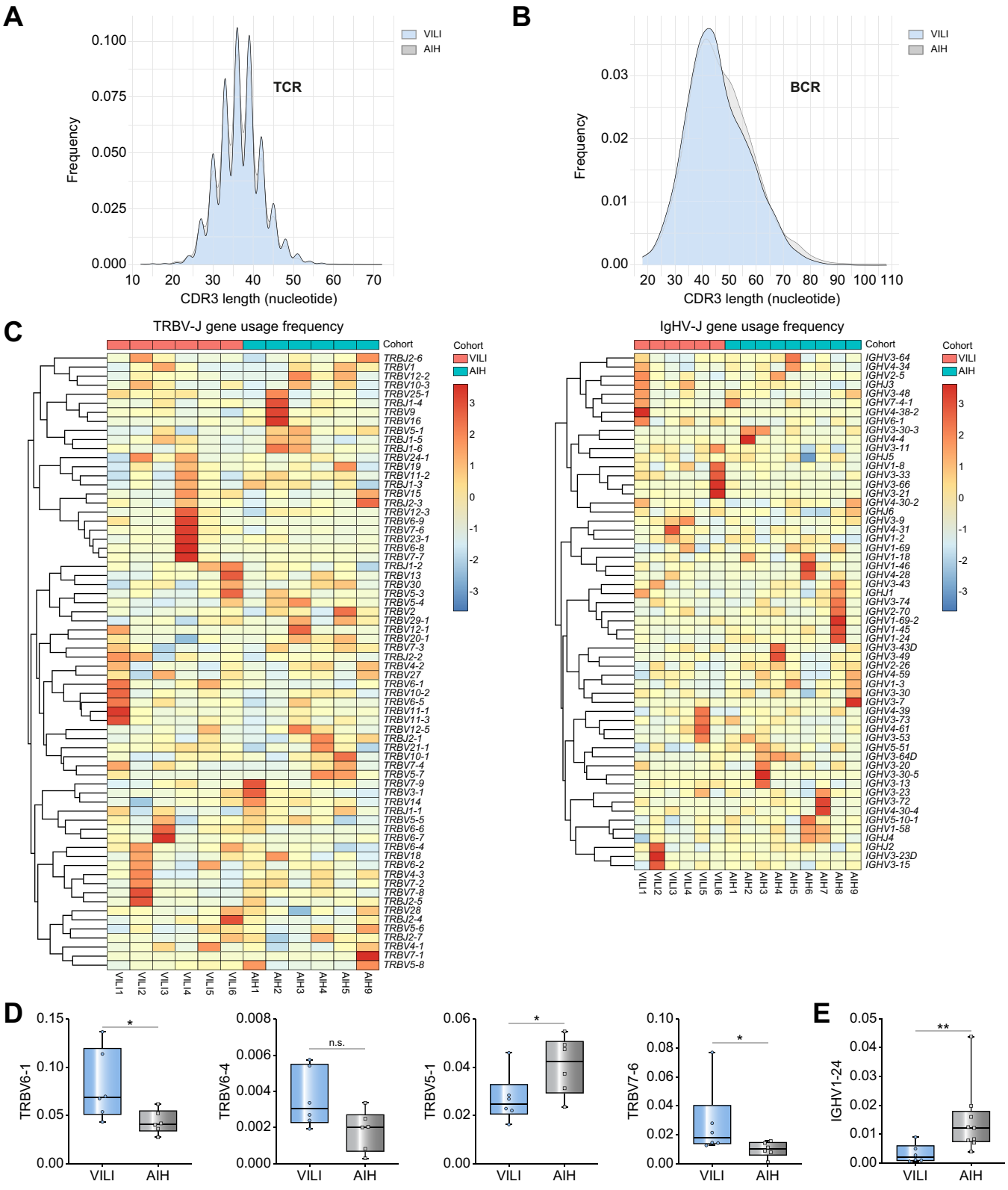

Fig. 4. Identical CDR3 length distribution but variations in TRBV-J and IgHV-J gene usage between patients with VILI and AIH. (A) CDR3 nucleotide length distribution of TCR repertoires of patients with VILI and AIH. (B) CDR3 nucleotide length distribution of BCR repertoires of VILI and AIH samples. (C) Heatmap of TCR-β chain and BCR CDR3 region variable and joining gene usage proportion in each sample. (D) Preferential usage of TRBV6-1, TRBV6-4, TRBV5-1, and TRBV7-6. (E) Preferential usage of IGHV1-24 in patients with AIH. For TCR analysis six patients with VILI and six patients with AIH, for BCR analysis six patients with VILI and nine patients with AIH were included. Each dot represents a patient. *p <0.05, **p <0.01, ***p <0.001 (two-group comparison: Wilcoxon rank-sum test). AIH, autoimmune hepatitis; BCR, B-cell receptor; CDR3, complementarity-determining region 3; IgHV-J, immunoglobulin heavy chain variable-joining; ns, not significant; TCR, T-cell receptor; TRBV-J, T-cell receptor beta variable-joining; VILI, vaccine-induced liver injury.

(summarised in Table S14).[7–9] The clinical, biochemical, histologic and partially serologic appearance of COVID-19 vaccine-induced hepatitis is similar to AIH.[10,11] However, it is unclear how these two diseases are related to each other. In addition, the pathophysiological mechanisms of COVID-19 vaccine-induced hepatitis are poorly understood, which prompted us to conduct this comparative study between VILI and AIH. All patients with VILI in our study showed a close temporal correlation between COVID-19 vaccination and hepatitis in the absence of other causes of acute liver injury. Although two patients were taking drugs potentially associated with liver injury (statin and lercanidipine/telmisartan), a causal relationship is unlikely, because these drugs usually cause liver toxicity within the first few weeks of use and our patients have been taking them for many years without previous adverse effects. Four of the six patients with VILI were ANA- or AAA-positive, including one with atypical AMA.[6] In addition, serum IgG levels were elevated in two patients. A total of 60% of our patients were classified as probable/definite AIH, according to the simplified criteria, which is only slightly lower than in previously published cohorts of VILI.[15] In contrast, all patients with AIH in our cohort had either ANA and/or ASMA/AAA and were all classified as probable/definite AIH according to the simplified criteria. Importantly, all patients with VILI responded well to steroid therapy or improved without therapy and remained in remission to date.

H&E morphology was very similar between VILI and AIH. A significant difference was found only in confluent necrosis, which was more extensive in VILI. Similarly, a previous report revealed a higher zone 3 necrosis in DI-AILH compared with AIH.[33] Interestingly, we found no difference between the two groups for eosinophilic infiltrates, a finding often associated with DILI.[33,34] Whole transcriptome analysis confirmed the close relationship between VILI and AIH. However, GSEA also revealed an overrepresentation of mitochondrial metabolism and oxidative stress-related pathways in VILI compared with AIH. These pathways have been mapped to hepatocytes and are important in DILI[27,28] and may indicate immunopathological similarities between VILI and DI-AILH. In contrast, we found an increase in pathways related to interferon-gamma signalling in AIH compared with VILI. Indeed, it is well known that interferon pathways are activated in AIH.[35,36] Interestingly, this interferon response still appears to be significantly higher in AIH than in VILI, although mRNA-based vaccination can also elicit interferon signalling.[37] Furthermore, VILI and AIH were clearly separated from patients with chronic HCV infection or ASH. However, this may be partly explained by the fact that patients with chronic HCV and ASH in our cohort had cirrhosis, which was not present in VILI and AIH.

Cellular analysis of liver inflammation by transcriptome analysis and multiplex immunofluorescence further showed that VILI was dominated by $CD8^+$ effector T cells, whereas $CD4^+$ effector T cells and B/plasma cells were more prominent in AIH. This is in line with earlier reports showing that activated cytotoxic $CD8^+$ T cells were highly enriched in the liver of patients with VILI.[9] Interestingly, we observed a similar dominance of $CD8^+$ effector T cells in DI-AILH, suggesting that VILI and DI-AILH are closely related and distinct from AIH.

TCR and BCR analysis revealed similar clone numbers and Shannon Diversity Index between VILI and AIH. Yet, we found that VILI had lower evenness in the TCR and BCR repertoires, indicating that VILI has expanded clones in T and B cell architecture compared with AIH. Therefore, vaccination induces a more restricted repertoire, as indicated by the increase of T cell clones in the top 1% of VILI. Additionally, we compared T cell clones from the liver biopsy of two patients with VILI with matched blood samples. Interestingly, many of the high frequency T cell clones in the liver were also found in the blood of the same patient. However, none of these shared clones matched to spike SARS-CoV-2 in a TCR database. Moreover, we observed a clonal overlap in the patient in whom $CD8^+$ T cells specific for a spike protein epitope ($S_{378-386}$) were depleted from PBMC.[9] Therefore, our data suggest that T cell clones that do not target a vaccine antigen may be involved in the pathogenesis of VILI. However, we cannot determine whether these high frequency T cells are activated in the liver and then spill over into the periphery or whether T cells from the periphery home to the liver to cause hepatitis.

Interestingly, in our gene usage analysis, we found a decrease in the rearranged TRBV6-1 and TRBV6-4 genes in AIH, in contrast to VILI. This is in line with earlier analysis of AIH, where also a decrease of TRBV6-1 and TRBV6-4 genes has been described.[32] The preferential usage of TRBV6 and TRBV20 family gene variants is a key feature of different subsets of mucosal associated invariant T (MAIT) cells.[38,39] Loss of MAIT cell subsets in the peripheral blood has been reported in a variety of autoimmune diseases and may be a characteristic for AIH. Furthermore, we observed a decrease in IGHV1-24 in VILI compared with AIH. In contrast, previous studies observed an enrichment of IGHV1-24 in B cell repertoires[40,41] after SARS-CoV-2 infection. However, no enrichment in IGHV1-24 was observed in IgH repertoires of healthy individuals after SARS-CoV-2 vaccination.[42]

COVID-19 vaccination is the most effective measure to prevent spreading and reduce mortality after SARS-CoV-2 infection. Moreover, the risk of liver injury during COVID-19 disease by far outweighs the risk of liver injury after vaccination.[43] Therefore, we strongly advocate vaccination during the pandemic. However, we need to be cautious of hepatitis as a rare side effect of vaccination and understand VILI better. We are aware of the rather small sample size of our study. However, besides some similarities between VILI and AIH, we found distinct differences between the two entities. TRBV-J gene usage showed that TRBV6-1 and TRBV6-4 were reduced only in the cohort with AIH, which has been described as typical for AIH.[32] Immune infiltration in VILI was also dominated by $CD8^+$ effector T cells, whereas $CD4^+$ effector T cells and $CD79a^+$ B and plasma cells were prominent in AIH. Mitochondrial metabolism and oxidative stress-related pathways were further upregulated in the cohort with VILI, in parallel with a more pronounced centrilobular necrosis. Although we cannot exclude that some VILI represent activation of latent AIH, our results suggest that in many individuals, VILI represents a separate disease entity, which is distinct from AIH, but more closely related to DI-AILH. Therefore, there is a good chance that many patients with VILI will recover completely and not develop long-term AIH.

Affiliations

[1]Institute of Pathology, University Hospital Basel, Basel, Switzerland; [2]Microscopy Core Facility, Department of Biomedicine, University of Basel, Basel, Switzerland; [3]Center for Virology and Vaccine Research, Beth Israel Deaconess Medical Center, Boston, MA, USA; [4]Department of Medicine II (Gastroenterology, Hepatology, Endocrinology and Infectious Diseases), Freiburg University Medical Center, Faculty of Medicine, University of Freiburg, Freiburg, Germany; [5]Faculty of Biology, University of Freiburg, Freiburg, Germany; [6]Institute for Surgical Pathology, Freiburg University Medical Center, University of Freiburg, Freiburg, Germany; [7]Core Facility for Histopathology and Digital Pathology, Medical Center, Faculty of Medicine, University of Freiburg, Freiburg, Germany; [8]Istituto Cantonale di Patologia, Locarno, Switzerland; [9]Innere Medizin, Spital Dornach, Dornach, Switzerland; [10]Department of Biomedical Sciences, Humanitas University, Pieve Emanuele, Milan, Italy; [11]IRCCS Humanitas Research Hospital, Rozzano, Milan, Italy; [12]Brain Tumor Immunotherapy Lab, Department of Biomedicine, University of Basel, Basel, Switzerland; [13]Department of Neurosurgery, University Hospital Basel, Basel, Switzerland; [14]Gastroenterology and Hepatology, University Centre for Gastrointestinal and Liver Diseases Basel, Switzerland; [15]Signalling Research Centres BIOSS and CIBSS, University of Freiburg, Freiburg, Germany; [16]Partner Site Freiburg, German Cancer Consortium (DKTK), Heidelberg, Germany; [17]Department of Biomedicine, University of Basel, Switzerland; [18]Department of Pathology, Dana Farber Cancer Institute, Boston, MA, USA; [19]Broad Institute of Harvard and MIT, Cambridge, MA, USA; [20]Faculty of Biomedical Sciences, Università Della Svizzera Italiana, Lugano, Switzerland; [21]Epatocentro Ticino, Lugano, Switzerland; [22]MowatLabs, Faculty of Life Sciences and Medicine, King's College London, King's College Hospital, London, UK

Abbreviations

AAAs, anti-actin antibodies; AIH, autoimmune hepatitis; ALP, alkaline phosphatase; ALT, alanine aminotransferase; AMAs, anti-mitochondrial antibody; ANAs, anti-nuclear antibody; ANCAs, anti-neutrophil cytoplasm antibodies; Anti-LC1, anti-liver cytosol type 1; Anti-LKM1, anti-liver-kidney microsome 1; Anti-SLA, anti-soluble liver antigen; ASMAs, anti-smooth muscle antibodies; ASH, alcoholic steatohepatitis; AST, aspartate aminotransferase; BCR, B-cell receptor; CDR3, complementarity-determining region 3; CODEX, CO-Detection by IndEXing; COVID-19, coronavirus disease 2019; DI-AILH, drug-induced autoimmune-like hepatitis; DILI, drug-induced liver injury; ; FFPE, formalin-fixed and paraffin-embedded; GGT, gamma-glutamyltransferase; GSEA, gene set enrichment analysis; IgH, immunoglobulin heavy chain; IgHV-J, immunoglobulin heavy chain variable-joining; lfc, log fold change; MAIT, mucosal associated invariant T; SARS-CoV-2, severe acute respiratory syndrome coronavirus 2; TCR, T-cell receptor; TRBV-J, T-cell receptor beta variable-joining; ULN, upper limit of normal; VILI, vaccine induced liver injury.

Financial support

This study was funded by the Botnar Research Centre for Child Health (FTC-2020-10) to AT, MSM, and GH and the Swiss National Science Foundation (SNSF; Grant No. 320030_189275) to MSM. SJ is supported by NIH DP2AI171139, and the Bill & Melinda Gates Foundation INV-002704. The sponsor of the study did not have any role in the study design, or collection, analysis, and interpretation of data.

Conflicts of interest

MSM has served as a consultant for ThermoFisher, Merck, GlaxoSmithKline, Janssen-Cilag, Roche, and Novartis and received speaker's honorary from Incyte Biosciences. GH is cofounder of Incephalo, not related to this project. Otherwise, the authors have no conflicts of interest to declare.

Please refer to the accompanying ICMJE disclosure forms for further details.

Authors' contributions

Conceptualisation: SU, MSM. Methodology: SU, MSM, ACB, EMB, SJ, CZ. Clinical data and patient integration: SU, MSM, JH, JV, LM, MM, IP, TH, LMT, AT, MH, CB, BTBP. Sample handling and processing: SU, ACB, CZ, IA, EMB, MM, IP, BC, MR, PB, AKS, JH, JV, LM, TH, LMT, AT, TB, MH, BB, MHH, CB, BTBP, MSM. Software: SU, ACB, CZ, IA, EMB. Formal analysis: SU, ACB, CZ, JY, IA, EMB, AKS, JH, JV, LM, TH, LMT, AT, MH, SJ, CB, BTBP, MSM. Investigation: SU, ACB, CZ, IA, EMB, JY, SJ, MSM. Resources: AT, MSM. Writing – original draft: SU, MSM. Writing – review and editing: all authors. Supervision: SU, MSM. Project administration: AKS, AT, MSM. Funding acquisition: AT, MSM, GH, SJ.

Data availability statement

The data of this study are available in Gene Expression Omnibus (https://www.ncbi.nlm.nih.gov/geo/) under GEO accession number GSE229459.

Acknowledgements

We would like to thank Jan Schneeberger for excellent technical assistance. We thank Dr Stéphanie Tissot and Dr Jonathan Thevenet from the Immune Landscape Laboratory of University Hospital of Lausanne for their support in GeoMx experiment and spatial transcriptome sequencing.

Supplementary data

Supplementary data to this article can be found online at https://doi.org/10.1016/j.jhep.2023.05.020.

References

Author names in bold designate shared co-first authorship.

[1] WHO Coronavirus (COVID-19) Dashboard, https://covid19.who.int/. Access Date 27 June 2023.

[2] **Li M**, **Wang H**, **Tian L**, **Pang Z**, Yang Q, Huang T, et al. COVID-19 vaccine development: milestones, lessons and prospects. Signal Transduct Target Ther 2022;7:146.

[3] Bril F, Al Diffalha S, Dean M, Fettig DM. Autoimmune hepatitis developing after coronavirus disease 2019 (COVID-19) vaccine: causality or casualty? J Hepatol 2021;75:222–224.

[4] Rocco A, Sgamato C, Compare D, Nardone G. Autoimmune hepatitis following SARS-CoV-2 vaccine: may not be a casuality. J Hepatol 2021;75:728–729.

[5] Londono MC, Gratacos-Gines J, Saez-Penataro J. Another case of autoimmune hepatitis after SARS-CoV-2 vaccination – still casualty? J Hepatol 2021;75:1248–1249.

[6] Ghielmetti M, Schaufelberger HD, Mieli-Vergani G, Cerny A, Dayer E, Vergani D, et al. Acute autoimmune-like hepatitis with atypical anti-mitochondrial antibody after mRNA COVID-19 vaccination: a novel clinical entity? J Autoimmun 2021;123:102706.

[7] Zin Tun GS, Gleeson D, Al-Joudeh A, Dube A. Immune-mediated hepatitis with the Moderna vaccine, no longer a coincidence but confirmed. J Hepatol 2022;76:747–749.

[8] Garrido I, Lopes S, Simoes MS, Rodrigo L, Lopes J, Carneiro F, et al. Autoimmune hepatitis after COVID-19 vaccine – more than a coincidence. J Autoimmun 2021;125:102741.

[9] **Boettler T**, **Csernalabics B**, Salie H, Luxenburger H, Wischer L, Alizei ES, et al. SARS-CoV-2 vaccination can elicit a CD8 T-cell dominant hepatitis. J Hepatol 2022;77:653–659.

[10] Codoni G, Kirchner T, Engel B, Villamil AM, Efe C, Stättermayer AF, et al. Histological and serological features of acute liver injury after SARS-CoV-2 vaccination. JHEP Rep 2023;5:100605.

[11] Efe C, Kulkarni AV, Terziroli Beretta-Piccoli B, Magro B, Stättermayer A, Cengiz M, et al. Liver injury after SARS-CoV-2 vaccination: features of immune-mediated hepatitis, role of corticosteroid therapy and outcome. Hepatology 2022;76:1576–1586.

[12] Kanduc D, Shoenfeld Y. Molecular mimicry between SARS-CoV-2 spike glycoprotein and mammalian proteomes: implications for the vaccine. Immunol Res 2020;68:310–313.

[13] Vojdani A, Kharrazian D. Potential antigenic cross-reactivity between SARS-CoV-2 and human tissue with a possible link to an increase in autoimmune diseases. Clin Immunol 2020;217:108480.

[14] Avci E, Abasiyanik F. Autoimmune hepatitis after SARS-CoV-2 vaccine: new-onset or flare-up? J Autoimmun 2021;125:102745.

[15] Roy A, Verma N, Singh S, Pradhan P, Taneja S, Singh M. Immune-mediated liver injury following COVID-19 vaccination: a systematic review. Hepatol Commun 2022;6:2513–2522.
[16] Manns MP, Czaja AJ, Gorham JD, Krawitt EL, Mieli-Vergani G, Vergani D, et al. Diagnosis and management of autoimmune hepatitis. Hepatology 2010;51:2193–2213.
[17] Hennes EM, Zeniya M, Czaja AJ, Dalekos GN, Krawitt EL, Bittencourt PL, et al. Simplified criteria for the diagnosis of autoimmune hepatitis. Hepatology 2008;48:169–176.
[18] Bjornsson ES, Medina-Caliz I, Andrade RJ, Lucerna MI. Setting up criteria for drug-induced autoimmune-like hepatitis through a systematic analysis of published reports. Hepatol Commun 2022;6:1895–1909.
[19] Fimiano F, D'Amato D, Gambella A, Marzano A, Saracco GM, Morgando A. Autoimmune hepatitis or drug-induced autoimmune hepatitis following Covid-19 vaccination? Liver Int 2022;42:1204–1205.
[20] Chen Y, Xu Z, Wang P, Li X, Shuai Z, Ye D, et al. New-onset autoimmune phenomena post-COVID-19 vaccination. Immunology 2022;165:386–401.
[21] Fontana RJ, Seeff LB, Andrade RJ, Björnsson E, Day CP, Serrano J, et al. Standardization of nomenclature and causality assessment in drug-induced liver injury: summary of a clinical research workshop. Hepatology 2010;52:730–742.
[22] Tiniakos DG, Brain JG, Bury YA. Role of histopathology in autoimmune hepatitis. Dig Dis 2015;33(Suppl. 2):53–64.
[23] Lohse AW, Sebode M, Bhathal PS, Clouston AD, Dienes HP, Jain D, et al. Consensus recommendations for histological criteria of autoimmune hepatitis from the international AIH Pathology group: results of a workshop on AIH histology hosted by the European reference network on hepatological diseases and the European society of Pathology. Liver Int 2022;42:1058–1069.
[24] Ishak K, Baptista A, Bianchi L, Callea F, Groote JD, Gudat F, et al. Histological grading and staging of chronic hepatitis. J Hepatol 1995;22:696–699.
[25] Hysenaj L, Little S, Kulhanek K, Gbenedio OM, Rodriguez L, Shen A, et al. SARS-CoV-2 infection studies in lung organoids identify TSPAN8 as novel mediator. bioRxiv 2021. https://doi.org/10.1101/2021.06.01.446640.
[26] Pollaci G, Gorla G, Potenza A, Carrozzini T, Canavero I, Bersano A, et al. Novel multifaceted roles for RNF213 protein. Int J Mol Sci 2022;23:4492.
[27] Mihajlovic M, Vinken M. Mitochondria as the target of hepatotoxicity and drug-induced liver injury: molecular mechanisms and detection methods. Int J Mol Sci 2022;23:3315.
[28] Yuan L, Kaplowitz N. Mechanisms of drug-induced liver injury. Clin Liver Dis 2013;17:507–518 vii.
[29] Aran D, Hu Z, Butte AJ. xCell: digitally portraying the tissue cellular heterogeneity landscape. Genome Biol 2017;18:220.
[30] **Black S**, **Phillips D**, **Hickey JW**, Kennedy-Darling J, Venkataraaman VG, Samusik N, et al. CODEX multiplexed tissue imaging with DNA-conjugated antibodies. Nat Protoc 2021;16:3802–3835.
[31] Pan MY, Li B. T cell receptor convergence is an indicator of antigen-specific T cell response in cancer immunotherapies. eLife 2022;11:e81952.
[32] Schultheiss C, Simnica D, Willscher E, Oberle A, Fanchi L, Bonzanni N, et al. Next-generation immunosequencing reveals pathological T-cell architecture in autoimmune hepatitis. Hepatology 2021;73:1436–1448.
[33] Qu LM, Wang SH, Yang K, Brigstock DR, Sun L, Gao R, et al. CD4(+) Foxp3(+)CD25(+/-) Tregs characterize liver tissue specimens of patients suffering from drug-induced autoimmune hepatitis: a clinical-pathological study. Hepatobiliary Pancreat Dis Int 2018;17:133–139.
[34] Suzuki A, Brunt EM, Kleiner DE, Miquel R, Smyrk TC, Andrade RJ, et al. The use of liver biopsy evaluation in discrimination of idiopathic autoimmune hepatitis versus drug-induced liver injury. Hepatology 2011;54:931–939.
[35] Terziroli Beretta-Piccoli B, Mieli-Vergani G, Vergani D. Autoimmmune hepatitis. Cell Mol Immunol 2022;19:158–176.
[36] Liberal R, de Boer YS, Heneghan MA. Established and novel therapeutic options for autoimmune hepatitis. Lancet Gastroenterol Hepatol 2021;6:315–326.
[37] **Arunachalam PS**, **Scott MKD**, **Hagan T**, Li C, Feng Y, Wimmers F, et al. Systems vaccinology of the BNT162b2 mRNA vaccine in humans. Nature 2021;596:410–416.
[38] **Reantragoon R**, **Corbett AJ**, Sakala IG, Gherardin NA, Furness JB, Chen Z, et al. Antigen-loaded MR1 tetramers define T cell receptor heterogeneity in mucosal-associated invariant T cells. J Exp Med 2013;210:2305–2320.
[39] Lepore M, Kalinichenko A, Colone A, Paleja B, Singhal A, Tschumi A, et al. Parallel T-cell cloning and deep sequencing of human MAIT cells reveal stable oligoclonal TCRbeta repertoire. Nat Commun 2014;5:3866.
[40] Voss WN, Hou YJ, Johnson NV, Delidakis G, Kim JE, Javanmardi K, et al. Prevalent, protective, and convergent IgG recognition of SARS-CoV-2 non-RBD spike epitopes. Science 2021;372:1108–1112.
[41] Nielsen SCA, Yang F, Jackson KJL, Ramona AH, Röltgen K, Jean GH, et al. Human B cell clonal expansion and convergent antibody responses to SARS-CoV-2. Cell Host Microbe 2020;28:516–525.e5.
[42] Kotagiri P, Mescia F, Rae WM, Bergamaschi L, Tuong ZK, Turner L, et al. B cell receptor repertoire kinetics after SARS-CoV-2 infection and vaccination. Cell Rep 2022;38:110393.
[43] **Wong CKH**, **Mak LY**, Au ICH, Lai FTT, Li X, Wan EYFW, et al. Risk of acute liver injury following the mRNA (BNT162b2) and inactivated (CoronaVac) COVID-19 vaccines. J Hepatol 2022;77:1339–1348.

Journal of Hepatology, Volume *79*

Supplemental information

Morphologic and molecular analysis of liver injury after SARS-CoV-2 vaccination reveals distinct characteristics

Sarp Uzun, Carl P. Zinner, Amke C. Beenen, Ilaria Alborelli, Ewelina M. Bartoszek, Jason Yeung, Byron Calgua, Matthias Reinscheid, Peter Bronsert, Anna K. Stalder, Jasmin D. Haslbauer, Juerg Vosbeck, Luca Mazzucchelli, Tobias Hoffmann, Luigi M. Terracciano, Gregor Hutter, Michael Manz, Isabelle Panne, Tobias Boettler, Maike Hofmann, Bertram Bengsch, Markus H. Heim, Christine Bernsmeier, Sizun Jiang, Alexandar Tzankov, Benedetta Terziroli Beretta-Piccoli, and Matthias S. Matter

Morphologic and molecular analysis of liver injury after SARS-CoV-2 vaccination reveals distinct characteristics

Sarp Uzun, Carl P. Zinner, Amke C. Beenen, Ilaria Alborelli, Ewelina M. Bartoszek, Jason Yeung, Byron Calgua, Matthias Reinscheid, Peter Bronsert, Anna K Stalder, Jasmine D Haslbauer, Juerg Vosbeck, Luca Mazzucchelli, Tobias Hoffmann, Luigi M. Terracciano, Gregor Hutter, Michael Manz, Isabelle Panne, Tobias Boettler, Maike Hofmann, Bertram Bengsch, Markus H. Heim, Christine Bernsmeier, Sizun Jiang, Alexandar Tzankov, Benedetta Terziroli Beretta-Piccoli and Matthias S. Matter

Table of Content

Supplementary Materials and Methods

Study design and patient selection

We collected six formalin-fixed and paraffin-embedded (FFPE) liver biopsy samples that showed liver injury after COVID-19 vaccination from the Institute of Pathology at the University Hospital Basel and the Institute of Pathology of Southern Switzerland in Locarno. For controls, we collected liver biopsies from patients with AIH (n = 9), alcoholic/non-alcoholic steatohepatitis (n = 17), and chronic hepatitis C viral infection with a high viral load (n = 13). Moreover, we included three patients with normal liver tissue by histology, who presented with a separate liver metastasis to the liver (2 with pancreatic carcinoma, 1 with urothelial carcinoma). For overlapping T-cell clone tracking, we additionally used the FFPE liver biopsy sample and blood samples of a published case “VILI patient Freiburg” (VILI_F).[1] For morphological comparison and multiplex immunohistochemistry, we collected liver biopsies from four drug-induced autoimmune-like hepatitis (DI-AILH). DI-AILH was caused in two patients by Infliximab and in two patients by Nitrofurantoin. All samples were evaluated by a consultant pathologist in the gastrointestinal/hepatology surgical pathologist team (MSM, JV, LT).

Clinical data collection

Reports included comprehensive laboratory and serological data that included anti-nuclear antibodies (ANA), anti-smooth muscle antibodies (SMA), anti-mitochondrial antibodies (AMA), anti-actin antibodies (AAA), anti-liver/kidney microsome type 1 (LKM-1), anti-liver cytosol type 1 (LC-1), anti-soluble liver antigen/liver pancreas antigen (anti-SLA/LP), anti-neutrophil cytoplasmic antibodies (ANCA), serum immunoglobulin G (IgG) and ceruloplasmin levels. Autoimmune liver serology was

evaluated according to local laboratory standards. Serological or PCR tests were performed for hepatitis virus A, B, C, D and E, Cytomegalovirus and Epstein–Barr virus.

Evaluation of liver injury

All patients were categorized for liver injury pattern by using the R-value, which is defined as serum alanine aminotransferase (ALT)/upper limit of normal (ULN) divided by serum alkaline phosphatase (ALP)/ULN. Liver injury was categorized as hepatocellular if the R ratio was >5, as mixed if 2-5, and as cholestatic if <2.[2]

Morphological evaluation of patient samples

Liver biopsies were evaluated by expert pathologists according to recommendations.[3-5] For Ishak grading, scores from 0-4 were assigned for periportal/periseptal interface hepatitis, focal spotty lytic necrosis/apoptosis/focal inflammation, and portal inflammation, while scores from 0-6 were assigned for confluent necrosis, as described.[4] Fibrosis was staged from 0-6 according to the Ishak scoring system.[4] The number of eosinophils in three lobules and portal tracts was counted and the following average number per lobule or portal tract was calculated.[6] Fibrosis was classified according to the Ishak scoring system.[4]

Total RNA isolation from FFPE Tissue Samples

25-30 µm thick FFPE tissue sections were obtained from each patient, deparaffinized with xylene, and total RNA and DNA were extracted simultaneously with the AllPrep DNA/RNA FFPE Kit (Qiagen, 80234) following the vendor's instructions. Final DNA and RNA concentrations were measured with Qubit dsDNA HS Assay Kit (ThermoFisher, Q32851) and RNA HS Assay Kits (ThermoFisher, Q32852), respectively.

Total RNA isolation from Frozen Blood Sample

The blood sample of VILI patient #5 was collected into a PAXgene Blood RNA tube (Qiagen, 762165) from the time of liver biopsy (10 days after liver biopsy). RNA isolation was performed with PAXgene Blood RNA Kit (Qiagen, 762174) according to vendor's instructions. Final RNA concentration was measured with Qubit RNA HS Assay Kits (ThermoFisher, Q32852).

Bulk RNA-Sequencing and Transcriptome Analysis

Extracted RNAs were used for bulk RNA-sequencing with the HTG Transcriptome Panel (HTG Molecular Diagnostics). First, the samples and controls were randomized by HTG prior to the processing to reduce any potential intra-plate bias. Samples were processed in accordance with HTG EdgeSeq processing. Briefly, the nuclease protection probes (NPPs) were added to the lysed samples in the sample plate in excess amount and hybridized to the target mRNA. Then S1 nuclease was added to digest non-hybridized RNA and excess NPPs, thus producing a stoichiometric amount of target mRNA NPP duplexes. After the S1 digestion was completed, the processed sample was transferred to a new 96-well microtiter plate, referred to as the stop plate, and S1 digestion was terminated by the addition of a termination solution followed by heat denaturation of S1 enzyme. Each processed sample from the stop plate was used as a template for PCR reactions. The library was prepared by using a PCR with OneTaq (New England Biolabs) and EdgeSeq PCR tag primers (HTG Molecular Diagnostics). Next, the PCR clean-up procedures were performed with AMPure cleanup beads (Beckman Coulter). The library was then quantified with AccuClear fluorescent dye (Biotium) and a Molecular Devices SpectraMax plate reader. All samples processed within this study had sufficient PCR product to be pooled for

sequencing. The sequencing was performed on the Illumina NextSeq 550 sequencer in accordance with the manufacturer's recommendations but also included two HTG custom sequencing primers. The sequenced data was provided in the form of FASTQ files and aligned to the list of probes in the panel with the HTG EdgeSeq parser version 5.3.0.7148. The parsed data undergoes post sequencing quality control steps using the HTG Reveal software version 4.0. First, a sufficient quality and quantity of RNA is ensured by imposing that a maximum of four per cent of reads are attributed to the positive process control probes for each sample. Second, a minimum of seven million reads per sample is required for sufficient read depth. Third, samples with low expression variability are detected and excluded. These are defined as samples where the median $\log_2$(CPM) of negative control probes is greater than two.

Differential Expression Analysis

Differential analysis was performed in R with DESeq2 version 1.34.0.[7] In accordance with the recommendation of HTG, the package's incorporated median of ratios normalization was used. The batches were inspected for unwanted variation using the RUVseq package (version 1.28). No significant correlation between batches and control signals could be found using a one-way ANOVA test. The normalized counts were prepared for visualization using a variance stabilizing transformation and further inspected for outliers in a principle component plot. One possible outlier was removed from the further analysis, completing the above cohort selection. A 3D principle component plot was created with Qlucore version 3.8 (Qlucore AB, Lund, Sweden) to explore the subgroups with optimal projection score for variance filtration. The differential expression itself was set up with a simple design formula containing only the variable of interest. Statistical significance was determined with the Wald test. Before the Benjamini-Hochberg false discovery rate adjustment, the number of genes

was automatically reduced by independent filtering. Additionally, the fold changes were adjusted with the apeglm shrinkage method.[8] Heatmaps were generated with the R pheatmap package version 1.0.12 using complete linkage for hierarchical clustering and row scaling for better visual differentiation.

Gene Set Enrichment Analysis

For the gene set enrichment analysis, the pre-ranked log2 fold changes were compared to multiple databases using the fGSEA package version 1.20. The databases were obtained from MSigDB and are the Hallmark gene sets (h.all.v7.5.1.symbols.gmt.txt), the curated gene sets (c2.all.v7.5.1.symbols.gmt.txt) as well as the ontology gene sets (c5.all.v7.5.1.symbols.gmt.txt). For visualization, at most 30 significantly up or down regulated gene sets were first selected and the relevant ones were used for plotting. All significant gene sets were shared in **Supplementary Table 6**.

Cell Type Enrichment Analysis

The xCell package version 1.1.0 was used to estimate cell type enrichment. The algorithm is insensitive to normalization, but requires a gene length adjustment. This is automatically obtained by means of HTG's targeted probe approach. Hence the use of CPM normalized counts is justified. The package's list of identifiable cells was reduced to the populations occurring in the liver. The results were filtered additionally when the cell type was not present in at least two samples. The heatmap contains row scaled values with Ward D2 hierarchical clustering. Differences are tested with a rank sum test and adjusted for false rate discoveries.

Quantitative real-time PCR (qPCR)

Extracted RNAs from FFPE samples of VILI, AIH, and normal liver samples were used (described above in the **Total RNA isolation from FFPE Tissue Samples**). Complementary DNA (cDNA) was synthesized from total RNA with SuperScript VILO cDNA Synthesis Kit (Thermo Fisher, 11754250). qPCR was carried out using SYBR green dye (FastStart Universal SYBR Green Master, 4913914001). GAPDH was used as a reference gene. The relative expression of TSPAN8 and RNF-213 was calculated by the $2^{-\Delta\Delta Ct}$ method and the normal liver cohort was used as a control.[9] The primer sets used in the study were included in **Supplementary Table 15**. The qPCR protocol was applied with the following incubation times: 50°C for 2 minutes; 95°C for 10 minutes; (95°C for 15 s/60°C for 1 min) × 40 cycles.

Spatial Transcriptomics with GeoMx Digital Spatial Profiler (DSP)

GeoMx DSP combines standard immunofluorescence techniques with digital optical barcoding technology to perform highly multiplexed, spatially resolved profiling experiments.[10] DNA oligonucleotide probes were designed to bind mRNA targets. From 5′ to 3′, each probe is comprised of a 35- to 50-nucleotide target complementary sequence, an ultraviolet (UV) photo cleavable linker and a 66-nucleotide indexing oligonucleotide sequence containing a unique molecular identifier (UMI), RNA ID sequence and primer binding sites.

Three FFPE tissue sections of 5-µm from liver biopsy tissue microarray (TMA) with VILI (n=6) and AIH (n=8) (TMA construction described below in the **Immunoprofiling with CO-Detection by indEXing (CODEX)**) were mounted on positively charged histology slides. Sections were incubated at 65 °C for 1 hour. Then, sections were deparaffinized in 3 xylol baths of 5 minutes and rehydrated in ethanol gradient from

100% EtOH 2 baths of 5 minutes, followed by 95% EtOH 5 minutes. Slides were then washed in 1X PBS. Antigen retrieval was carried out with Tris-EDTA pH 9.0 buffer at 100°C for 20 minutes at low pressure. Slides were first immersed into hot water for 10 seconds and then immersed into Tris-EDTA buffer. The cooker vent kept open during the procedure to ensure low pressure and it was allowed to reach 100°C. Slides were then washed with 1X PBS, and incubated in proteinase K containing PBS (1ug/ml) for 15 minutes at 37°C and washed again in 1X PBS. Tissue were post-fixed in 10% neutral-buffered formalin (NBF) for 5 minutes, washed two times 5 minutes in NBF stop buffer (0.1M Tris Base, 0.1M Glycine) and finally one time in 1X PBS. The mix of Whole Transcriptome Atlas probes (WTA, Nanostring) was dropped on each section and covered with HybriSlip Hybridization Covers. Slides were then incubated for hybridization overnight at 37°C in a Hyb EZ II hybridization oven (Advanced cell Diagnostics). The day after, HybriSlip covers were gently removed and 25 minutes stringent washes were performed twice in 50% formamide and 2X saline sodium citrate (SSC) at 37 °C. Tissues were washed for 5 min in 2× SSC, then blocked in Buffer W (Nanostring Technologies) for 30 min at room temperature in a humidity chamber. Next, 500 nM Syto83 and antibodies targeting CD3 (BioRad, clone CD3-12), CD20 (Novus, clone IGEL/773) and Arginase (Cell Signaling, clone D4E3M) in Buffer W were applied to each section for 1 h at room temperature. Slides were washed twice in fresh 2× SSC then loaded on the GeoMx DSP.

Entire slides were imaged at ×20 magnification and morphologic markers were used to select Region Of Interest (ROI) either using circle or organic shapes. Automatic segmentation of ROI based on Arginase+ markers were used to defined Area of Illumination (AOIs). This allowed to separate liver cells (Arginase+) and cells around liver. A total of 59 AOIs were exposed to 385 nm light (UV), releasing the indexing oligonucleotides which were collected with a microcapillary and deposited in a 96-well

plate for subsequent processing. The indexing oligonucleotides were dried down overnight and resuspended in 10 µl of DEPC-treated water.

Sequencing libraries were generated by PCR from the photo-released indexing oligos and AOI-specific Illumina adapter sequences, and unique i5 and i7 sample indices were added. Each PCR reaction used 4 µl of indexing oligonucleotides, 4 µl of indexing PCR primers, 2 µl of Nanostring 5X PCR Master Mix. Thermocycling conditions were 37 °C for 30 min, 50 °C for 10 min, 95 °C for 3 min; 18 cycles of 95 °C for 15 s, 65 °C for 1 min, 68 °C for 30 s; and 68 °C for 5 min. PCR reactions were pooled and purified twice using AMPure XP beads (Beckman Coulter, A63881), according to the manufacturer's protocol. Pooled libraries were single-sequenced at 27 base pairs and with the single-index workflow on an Illumina NovaSeq S4 instrument. FastQ files were converted into DCC files according to manufacturer's pipeline. Digital Count Conversion files were imported back into the GeoMx DSP instrument for QC and data analyses using GeoMx DSP analysis suite version 2.4.2.2 (Nanostring).

GeoMx DSP Differential Expression Analysis and Gene Set Enrichment Analysis

Following standard preprocessing and quality control of data as outlined by NanoString guidelines, differential gene expression analysis was performed on the quantile normalized count data in R with limma version 3.52.4. The simple design model was set up to compare ROIs between our VILI and AIH cohorts, taken across portal and central regions of the liver. Statistical significance was determined using an empirical Bayes t-test, as described by the limma package. All P-values were adjusted using Benjamini-Hochberg. A full list of differentially expressed genes can be accessed in **Supplementary Table 7**.

For gene set enrichment analysis, pre-ranked log2 fold change values were mapped to MSigDB gene sets using fgsea version 1.22.0. The same aforementioned gene sets used in our analysis of bulk transcriptomic profiling were used here (hallmark, curated, and ontology gene sets). To visualize pathways and confirm our findings, the same enriched pathways plotted in our bulk RNA-sequencing analysis are also pulled and plotted from the GeoMx dataset. All significant gene sets are shared in **Supplementary Table 8**.

PBMC Isolation, Enrichment of spike-specific CD8$^+$ T cells and RNA Isolation from Blood Samples of VILI_F

PBMCs (Peripheral blood mononuclear cells) were isolated with density gradient centrifugation from anticoagulated blood samples of patient VILI_F which were collected from three different time points. SARS-CoV-2 spike peptide (S378-386: KCYGVSPTK) was synthesized (Genaxxon Bioscience), loaded on HLA-A∗03:01 easYmers® (immunAware) and subsequently conjugated with phyocerythrin (PE)-streptavidin (Agilent). PBMCs were incubated with phyocerythrin (PE)-conjugated tetramerized S378-386-loaded HLA-A∗03:01 easYmers as described before.[1] Virus-specific CD8$^+$ T-cells were enriched by MACS technology using anti-PE beads. The remaining CD8$^+$ T-cells which were depleted from Spike (A∗03/S378)-specific CD8$^+$ T-cells were used for TCR sequencing. For this, total RNA was isolated from CD8$^+$ T-cells with AllPrep DNA/RNA Mini Kit (Qiagen, 80204) according to vendor's instructions.

T-Cell Receptor (TCR) and B-Cell Receptor (BCR) Library Preparation and Sequencing

RNAs extracted from FFPE samples of VILI and AIH, from frozen blood sample of VILI patient #5 and from $CD8^+$ T-cells of VILI_F were used to prepare the libraries for TCR and BCR sequencing. cDNA was synthesized from RNA by using the SuperScript VILO cDNA Synthesis Kit (Invitrogen, 11754250) and Ion Torrent NGS Reverse Transcription Kit (ThermoFisher, A45003) for TCR and BCR sequencing, respectively. T-cell and B-cell RNA was quantified by qPCR with TaqMan Gene Expression Assay, CD247 (20X, Hs00167901_m1) and CD19 (20X, Hs01047413_g1). Final input was normalized to 1 ng of T- and B-cell derived RNA per sample. For samples with low T- and B-cell counts, maximum RNA input was loaded for library preparation. Next-Generation Sequencing (NGS) libraries were prepared using the Oncomine TCR Beta-SR RNA Assay (ThermoFisher, A39359) and the Oncomine BCR IGH SR RNA Assay (ThermoFisher, A45484) according to manufacturer's instructions. Amplified and barcode ligated libraries were purified with AMPure XP Reagent (Beckman Coulter, A63880) and quantified with the Ion Universal Library Quantitation Kit (ThermoFisher, A26217). The library pool was prepared by combining equal volumes of libraries at 50 pmol/L concentration and loaded into Ion 550™ Chip (ThermoFisher, A34537). The libraries were sequenced on an Ion GeneStudio S5 Prime Sequencer (ThermoFisher).

TCR and BCR Sequencing Data Analysis

Sequencing analysis was performed on Ion Reporter Software, Version 5.18 (ThermoFisher). General immune repertoire metrics such as Shannon diversity index and evenness were calculated to describe the diversity of the T- and B-cell clones in the tissues. Shannon diversity index (H) of each patient was defined with the formula:

$$H = -\sum_{i=1}^{N} \quad Pi \log_2 (Pi)$$

where the sum is taken over N number of different clones and Pi is the frequency of the clone i. Evenness, which has values between 0 and 1, denotes the distribution of T-/B-cell clones in a single sample. Values close to 0 indicate an unbalanced clone distribution with dominant high-frequency clones, while values close to 1 indicate a balanced distribution of clones.[11] Total clonal space analysis of T- and B-cell clones was done by frequency classification of T- and B-cell clones according to their ranked abundance in the total immune repertoire in each sample. The clonal space was divided into top 1%, top 1-2%, top 2-5%, and top >5% as shown previously[11, 12] and the total frequency of each clonal space was calculated by summing up the frequency of each clone found in the respective space. Each T-cell with the same variable-joining regions and complementarity-determining region 3 (CDR3) is defined as a T-cell clone. Shared T-cell clone analysis between samples was performed with the R Studio Stringdist package[13] by calculating the Levenstein distance between CDR3 amino acid sequences. TCR convergence was defined as T-cells with identical TCRs and the same amino acid sequences but with different nucleotide sequences. CDR3 nucleotide length distribution of T- and B-cell clones were plotted with R Studio Version 4.1.2. ggplot 2.[14] The heatmap for TCR beta chain variable-joining gene (TRBV-J) and Ig heavy chain variable-joining gene (IgHV-J) usage was generated by using the frequency of each T-cell or B-cell clone in the VILI or AIH patient. For plotting, R pheatmap package version 1.0.12 was used with row scaling for better visual differentiation. For epitope prediction, TCR CDR3β amino acid sequences from VILI cases were uploaded into a web-based epitope prediction tool (http://tools.iedb.org/tcrmatch/). Highest match prediction (>0.97) was selected as the filtering level and CDR3β-matching spike glycoprotein epitopes were summarized in **Supplementary Table 11**.

Immunoprofiling with CO-Detection by indEXing (CODEX)

We reconstructed two tissue blocks by using the FFPE samples of VILI and AIH, with normal liver and tonsils as controls. First, tissue blocks were melted and approximately 0.5 mm of tissue was cut from each liver needle biopsy sample. Then, these biopsy sample pieces were aligned next to each other and re-embedded into two tissue blocks. From each tissue block, two 4µm sections were taken on poly-L-lysine coated coverslips for multiplex immunohistochemistry and one 2 µm section for H&E. Tissue sections were stained according to the protocol supplied by the manufacturer (Akoya Biosciences, CODEX User Manual Rev C) with slight modifications. For heat-induced epitope retrieval, tissue sections were incubated in citrate buffer (pH: 6.0) for 15 minutes at 98^{o}C in a laboratory-type microwave. The tissue sections were incubated with the primary antibody cocktail for 3 hours at room temperature. The tissues were fixed with 1.6% PFA for 10 minutes, 100% methanol for 5 minutes, and CODEX fixative reagent for 20 minutes. Stained tissues were stored in the storage buffer at 4^{o}C until image acquisition. The image acquisition was done with a Leica DMi8 microscope with a 20x objective (HC Plan-Apo 20x/0.8Air) with a Prime 95B camera and Leica LAS X Software Version 5.1.0. Data was acquired with 9 Z-steps of 1.5 µm. For focus setup, a focus map was created by selecting 5-7 focus points per tissue and using autofocus mode. The reagents and antibodies used in the CODEX were listed in **Supplementary Table 16**.

CODEX Data Preprocessing

Fiji[15] was used for image preprocessing. Briefly, images from a single tile were collected (including all 4 channels and 9 Z-steps) and a rolling ball subtraction with a radius of 15 pixels was performed. The z-stack was maximum projected for each channel separately. A registration of cells between consecutive cycles based on DAPI

(4′,6-diamidino-2-phenylindole) was performed using MultiStackReg plugin[16] and the same correction was propagated on the remaining channels. Tiles were stitched using Grid/Collection stitching plugin.[17] Due to high autofluorescence in the liver tissue, blank cycles (only DAPI channel without another staining with the same exposure time in the corresponding channels) were acquired and subtracted from the remaining cycles.

CODEX Data Analysis

Multichannel tiff was further saved as a pyramidal file using the Kheops plugin[18], and the image was opened in QuPath.[19] Stainings were validated by visual inspection and from the proteinatlas.[20] Tonsils and normal liver were used for the staining validation and were not included in the data analysis. Cell segmentation was done on nuclear channel DAPI using StarDist2D[21] plugin within QuPath with the following parameters: probability threshold: 0.7, pixel size: 0.5 and cell expansion: 2.0 using the model dsb2018_heavy_augment.pb. A table with the mean intensity of each marker per cell was exported and further used in OMIQ software (https://omiq.ai). Single-cell data was clustered using Phenograph algorithm[22] with k=20 into 51 phenotypes. Clustering was based on the following markers: arginase, CD3, CD4, CD8, CD20, CD68, CD79a, CK19, FoxP3, and Ki67. To validate clusters, each cell was color-coded based on its cluster-ID, overlaid on a multichannel image, and visually inspected. Clusters with similar expression patterns after visual verification were merged and, additionally, clusters with unspecific staining were excluded. The final number of clusters was 11. Portal and central veins were annotated on the tissue based on CD31 from fluorescent staining and corresponding H&E image. Those regions were expanded by 150 µm to delineate portal and central vein regions. Distance from each cell to the nearest annotation was calculated.

The antibody panel for DI-AILH consisted of 9 antibodies to evaluate immune cell composition within portal and centrilobular regions. QuPath[17] was used to train object classifiers based on cell features such as mean, minimum, maximum, standard deviation of intensity values. One classifier was trained to distinguish $CD8^+$, $CD4^+$, $CD79a^+$ cells, separate classifiers were trained for $CD3^+$ and $Foxp3^+$ cells. Composite classifier was applied to extract different cell types.

All data were analyzed on raw pixel values and brightness and contrast were adjusted for visualization. Final figures were prepared using Fiji.

Statistical Analysis

The data were represented as mean and standard error of mean or median and min-max values. Unpaired two-tailed Student *t*-test and Wilcoxon rank-sum test was used for two group comparisons. Spearman rank correlation test was used for all correlation analyses. The statistical tests were specified in the respective figure legend. A two-tailed *p* value < 0.05 was used to infer statistical significance. All graphs and statistical testing were done using GraphPad Prism version 9.2.0 and R Studio Version 4.1.2.

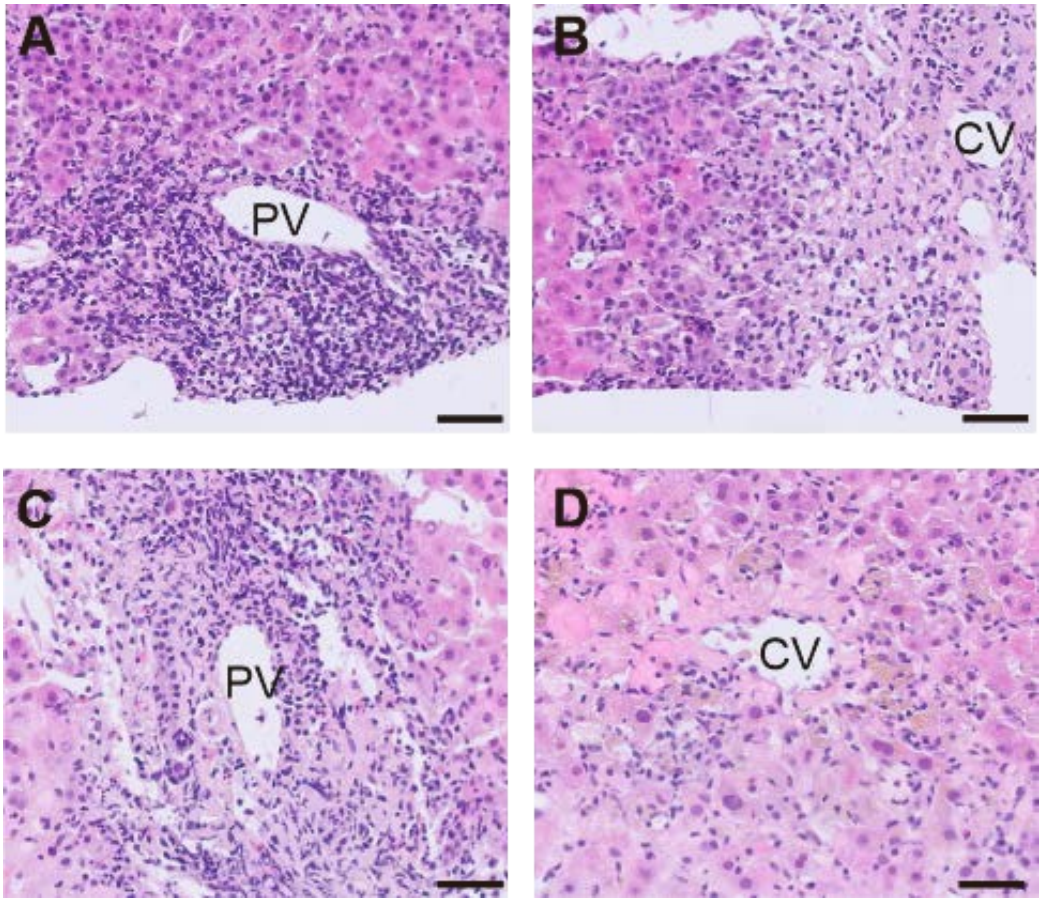
A
PV
B
CV
C
PV
D
CV

Supp. Fig 1. Representative image showing liver morphology from VILI and AIH. **(A)** Portal tract of VILI and **(C)** AIH with portal inflammation and interface hepatitis. **(B)** Extensive centrilobular necrosis of VILI and **(D)** less pronounced centrilobular necrosis of AIH, both with intralobular inflammation. PV = portal vein, CV = central vein. Bar = 50 µm.

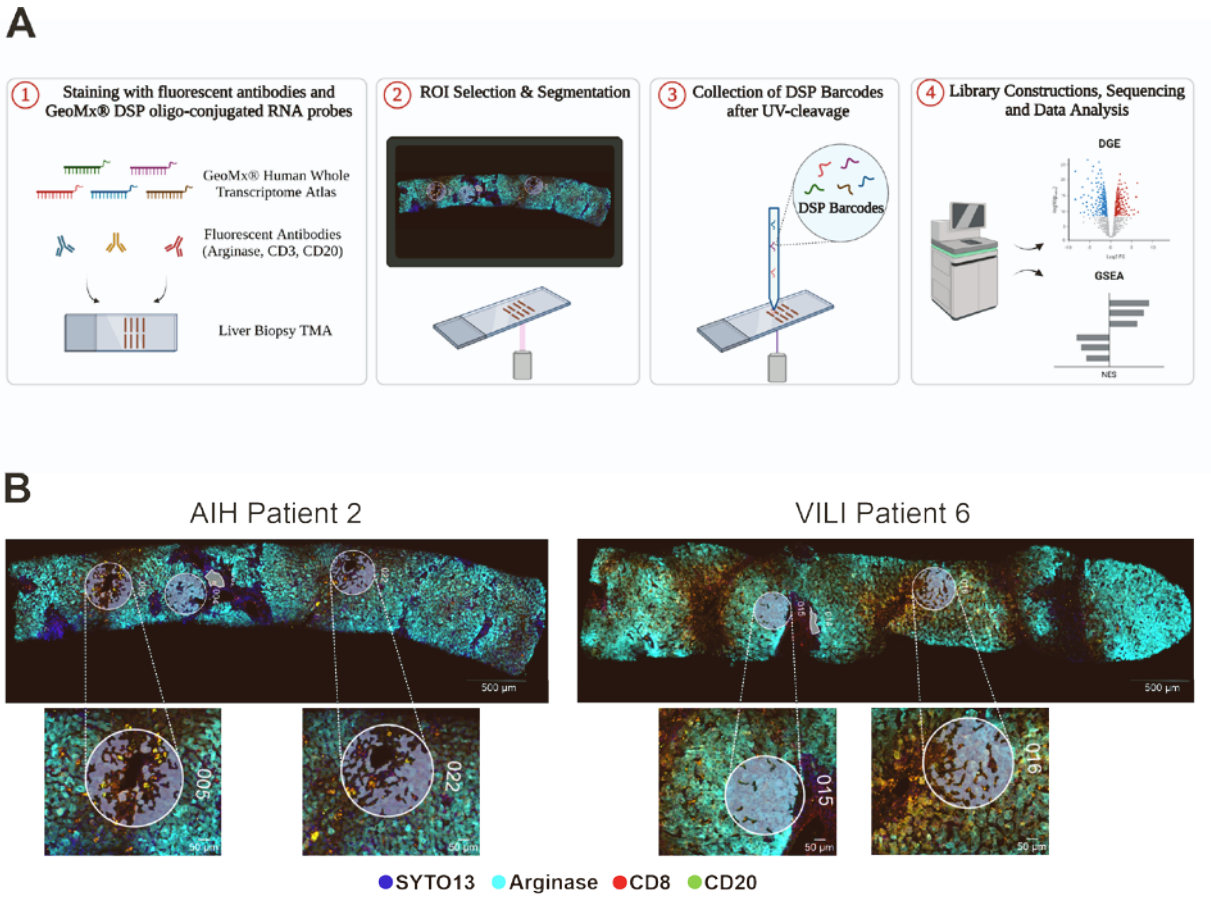
A
1 Staining with fluorescent antibodies and GeoMx® DSP oligo-conjugated RNA probes
GeoMx® Human Whole Transcriptome Atlas
Fluorescent Antibodies (Arginase, CD3, CD20)
Liver Biopsy TMA
2 ROI Selection & Segmentation
3 Collection of DSP Barcodes after UV-cleavage
DSP Barcodes
4 Library Constructions, Sequencing and Data Analysis
DGE
GSEA
NES
B
AIH Patient 2
VILI Patient 6
500 µm
005
022
015
016
50 µm
SYTO13 Arginase CD8 CD20
C
CYP3A4
CYP1A2
SUPT7L
HSPA5
TOB1
G6PC1
MGST1
CDHR2
PZP
IFITM1
FTCD
CXCL10
CCDC13
XAF1
TNFSF10
SCD
HMGCLL1
FBP1
COMT
CYP2C8
SLC43A3
POLD4
-log10 adjusted p-value
log2 fold change
D
NS
padj < 0.05
HALLMARK_OXIDATIVE_PHOSPHORYLATION
HSIAO_LIVER_SPECIFIC_GENES
GOBP_ALPHA_AMINO_ACID_METABOLIC_PROCESS
GOBP_CELLULAR_AMINO_ACID_METABOLIC_PROCESS
WP_IL4_SIGNALING_PATHWAY
ICHIBA_GRAFT_VERSUS_HOST_DISEASE_35D_UP
WIELAND_UP_BY_HBV_INFECTION
HP_ABNORMALITY_OF_THE_LYMPH_NODES
GOBP_T_CELL_MEDIATED_CYTOTOXICITY
GOBP_ANTIGEN_PROCESSING_AND_PRESENTATION_OF_EXOGENOUS_PEPTIDE_ANTIGEN
GOBP_LEUKOCYTE_MEDIATED_CYTOTOXICITY
GOBP_NATURAL_KILLER_CELL_MEDIATED_IMMUNITY
HP_ABNORMAL_ERYTHROCYTE_SEDIMENTATION_RATE
REACTOME_INTERFERON_GAMMA_SIGNALING
HP_ABNORMAL_B_CELL_MORPHOLOGY
GOBP_INTERLEUKIN_6_PRODUCTION
GOBP_POSITIVE_REGULATION_OF_LEUKOCYTE_CELL_CELL_ADHESION
HALLMARK_INTERFERON_GAMMA_RESPONSE
HALLMARK_INTERFERON_ALPHA_RESPONSE
KEGG_NATURAL_KILLER_CELL_MEDIATED_CYTOTOXICITY
WP_MICROGLIA_PATHOGEN_PHAGOCYTOSIS_PATHWAY
GOBP_IMMUNE_RESPONSE_REGULATING_CELL_SURFACE_RECEPTOR_SIGNALING_PATHWAY
PID_RHOA_REG_PATHWAY
BLANCO_MELO_HUMAN_PARAINFLUENZA_VIRUS_3_INFECTION_A594_CELLS_UP
BLANCO_MELO_BRONCHIAL_EPITHELIAL_CELLS_INFLUENZA_A_DEL_NS1_INFECTION_UP
BROWNE_INTERFERON_RESPONSIVE_GENES
SANA_RESPONSE_TO_IFNG_UP
Pathway
0 2 4
Normalized Enrichment Score

Supp. Fig 2. Spatial Transcriptomics of VILI and AIH Patient Samples

(A) GeoMx workflow. The figure was created in BioRender.com (2023) **(B)** 59 ROIs were selected from 3 different tissue microarrays (TMAs) having VILI (n=6) and AIH (n=8) biopsy samples. Automatic segmentation of Arginase^{+} cells in ROIs was performed. Bar=500 μm for whole liver biopsy; bar=50 μm for ROIs **(C)** Volcano plot shows the differentially expressed genes between VILI and AIH hepatocytes **(D)** Hepatocytes from VILI show significant enrichment of oxidative and metabolic pathways. Only pathways that were visualized in the bulk-RNA-sequencing enrichment analysis are presented.

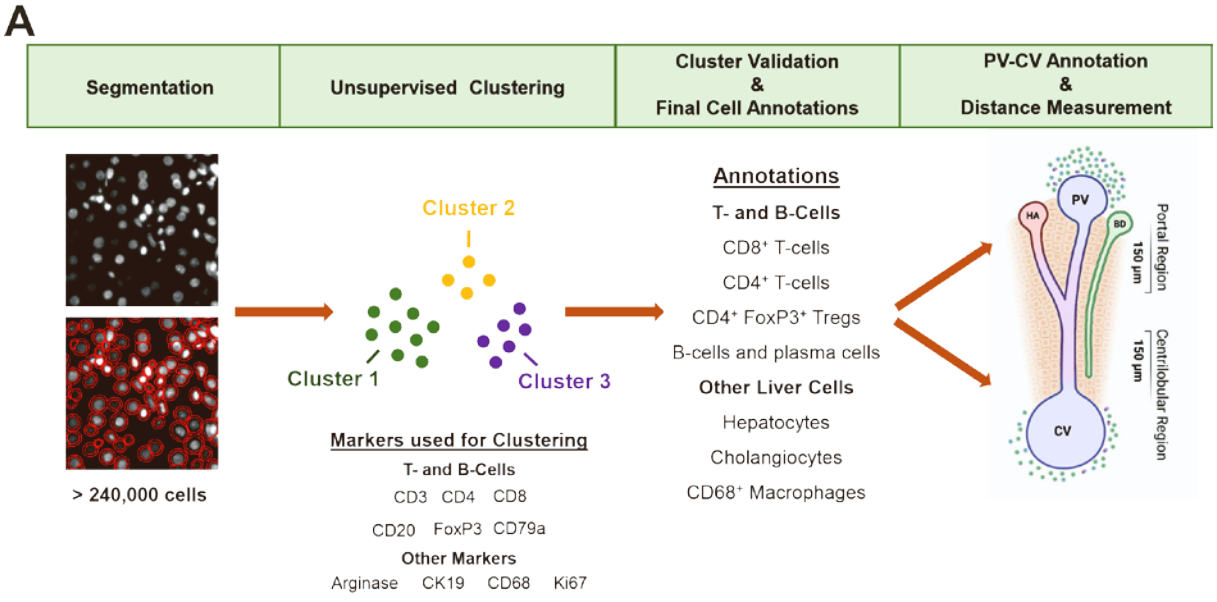
A
Segmentation
Unsupervised Clustering
Cluster Validation & Final Cell Annotations
PV-CV Annotation & Distance Measurement
> 240,000 cells
Cluster 1
Cluster 2
Cluster 3
Markers used for Clustering
T- and B-Cells
CD3 CD4 CD8
CD20 FoxP3 CD79a
Other Markers
Arginase CK19 CD68 Ki67
Annotations
T- and B-Cells
CD8+ T-cells
CD4+ T-cells
CD4+ FoxP3+ Tregs
B-cells and plasma cells
Other Liver Cells
Hepatocytes
Cholangiocytes
CD68+ Macrophages
PV
HA
BD
CV
150 µm
Portal Region
Centrilobular Region

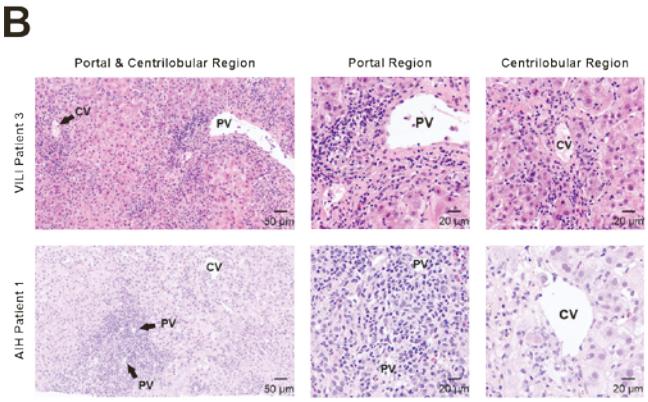
B
Portal & Centrilobular Region
Portal Region
Centrilobular Region
VILI Patient 3
AIH Patient 1
CV
PV
50 µm
20 µm

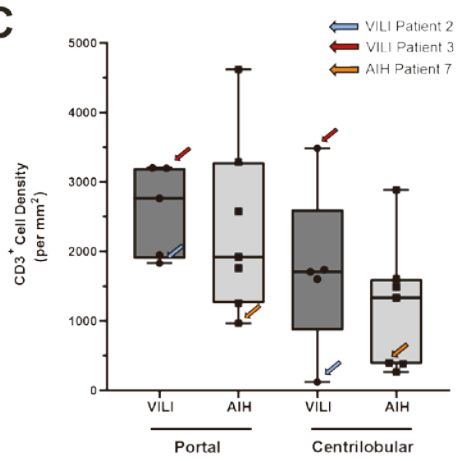
C
VILI Patient 2
VILI Patient 3
AIH Patient 7
CD3+ Cell Density (per mm2)
5000
4000
3000
2000
1000
0
VILI
AIH
VILI
AIH
Portal
Centrilobular

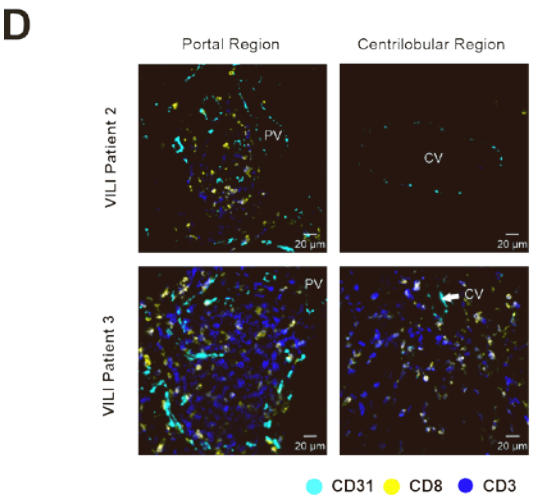
D
Portal Region
Centrilobular Region
VILI Patient 2
VILI Patient 3
PV
CV
20 µm
CD31 CD8 CD3

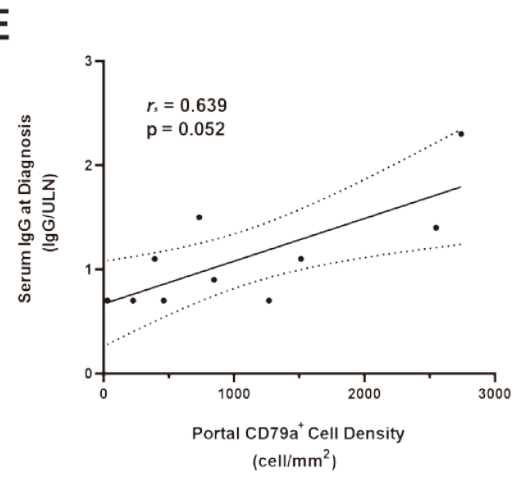
E
rs = 0.639
p = 0.052
Serum IgG at Diagnosis (IgG/ULN)
3
2
1
0
0
1000
2000
3000
Portal CD79a+ Cell Density (cell/mm2)

Supp. Fig. 3. CODEX Analysis of VILI and AIH Patient Samples

(A) CODEX data analysis workflow. CV: central vein; PV: portal vein, HA: hepatic artery, BD: Bile duct. A part of the figure was adapted from “hepatic sinusoid”, by BioRender.com (2022). **(B)** Hematoxylin and eosin staining of portal and centrilobular region of VILI patient #3 and AIH patient #1. CV: central vein; PV: portal vein. **(C)** $CD3^+$ cell density in the portal and centrilobular region of VILI and AIH patients. Blue arrows indicate VILI patient #2, red arrows indicate VILI patient #3, orange arrows indicate AIH patient #7. **(D)** $CD3^+$ and $CD3^+$ $CD8^+$ cell distribution in the portal and centrilobular region of VILI and AIH patients. Cyan(CD31), blue(CD3), yellow(CD8). CV: central vein; PV: portal vein. **(E)** Correlation analysis between IgG serum level at diagnosis (IgG/ULN) and portal B-cell ($CD79a^+$) density. The black line shows the linear regression line and dotted lines represent the 95% confidence interval upper and lower limits (Spearman rank correlation test). VILI cohort, *n*=5; AIH cohort, *n*=7. Each dot represents a patient.

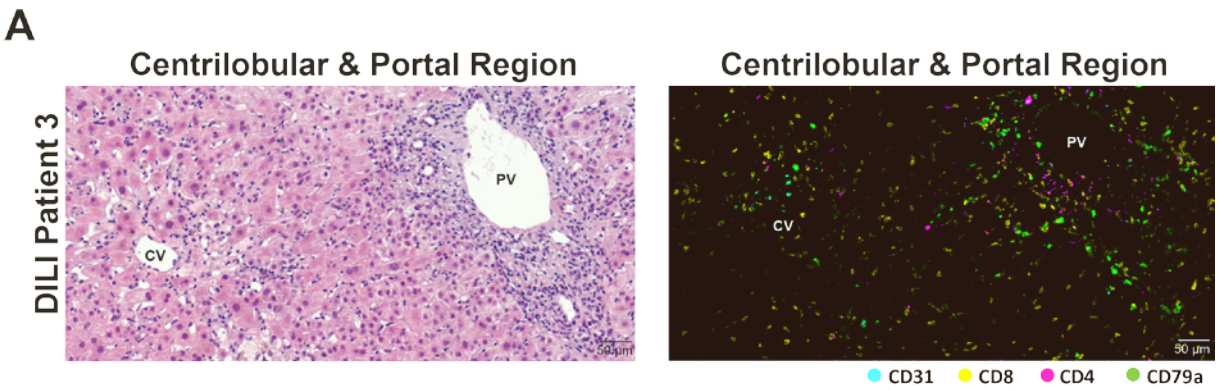
A
Centrilobular & Portal Region
Centrilobular & Portal Region
DILI Patient 3
PV
CV
PV
CV
50 μm
50 μm
CD31
CD8
CD4
CD79a

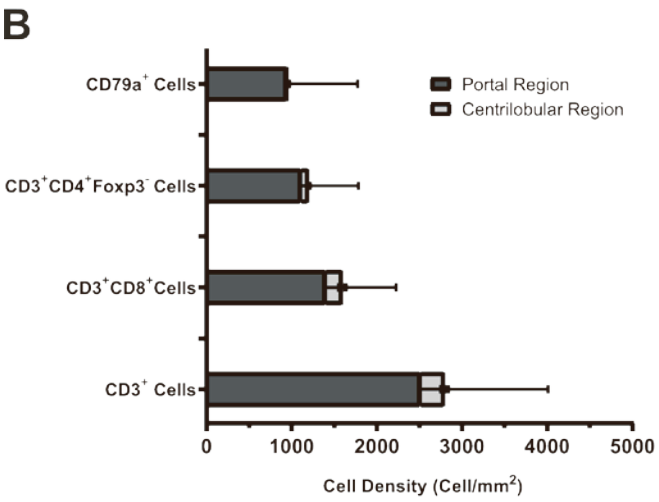
B
CD79a+ Cells
CD3+CD4+Foxp3- Cells
CD3+CD8+Cells
CD3+ Cells
Portal Region
Centrilobular Region
0
1000
2000
3000
4000
5000
Cell Density (Cell/mm2)

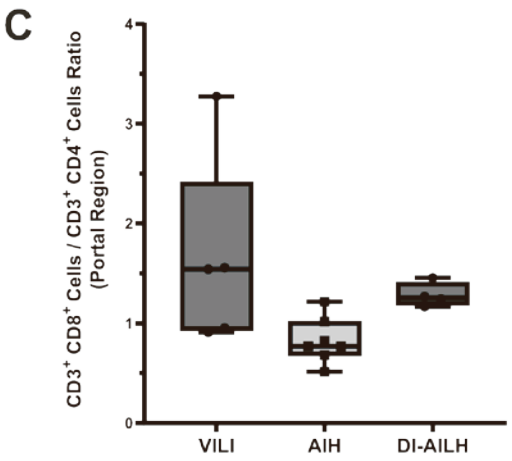
C
CD3+ CD8+ Cells / CD3+ CD4+ Cells Ratio
(Portal Region)
0
1
2
3
4
VILI
AIH
DI-AILH

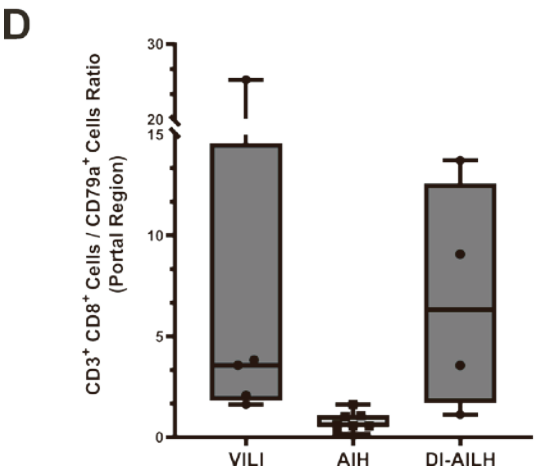
D
CD3+ CD8+ Cells / CD79a+ Cells Ratio
(Portal Region)
0
5
10
15
20
30
VILI
AIH
DI-AILH

Supp. Fig. 4. CODEX Analysis of DI-AILH

(A) H&E and CODEX staining of portal and centrilobular region of DI-AILH patient #3. CV: central vein; PV: portal vein. Cyan (CD31), yellow (CD8), pink (CD4) and Green ($CD79a^+$). **(B)** Immune cell distribution in the portal and centrilobular region of DI-AILH samples. Bar graphs indicate mean and standard error of mean (SEM) of immune cell densities (cells/mm^2). **(C)** Ratio of $CD3^+$ $CD8^+$/$CD3^+$ $CD4^+$ T cells in the portal region of VILI, AIH and DI-AILH samples. **(D)** Ratio of $CD3^+$ $CD8^+$/$CD79a^+$ T cells in the portal region of VILI, AIH and DI-AILH samples.

A

TCR Spectratyping Plots

VILI Patient 2

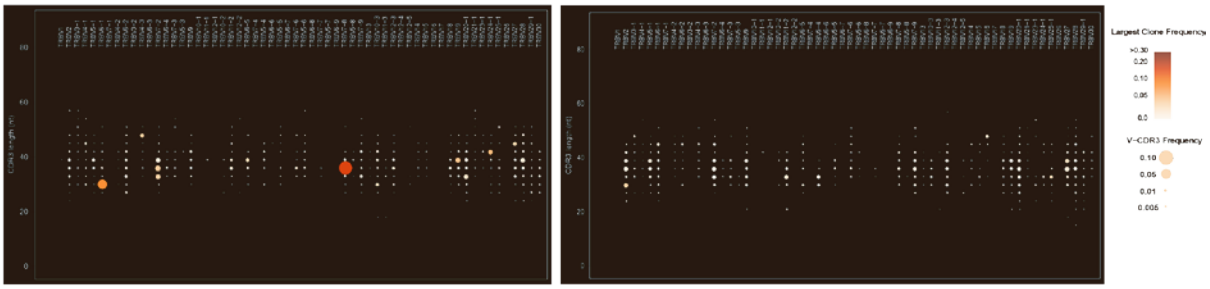

AIH Patient 2

VILI Patient 6

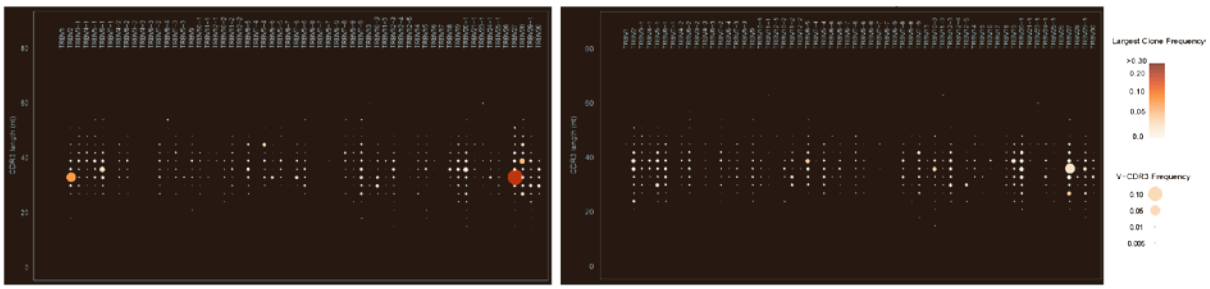

AIH Patient 3

B

BCR Spectratyping Plots

VILI Patient 2

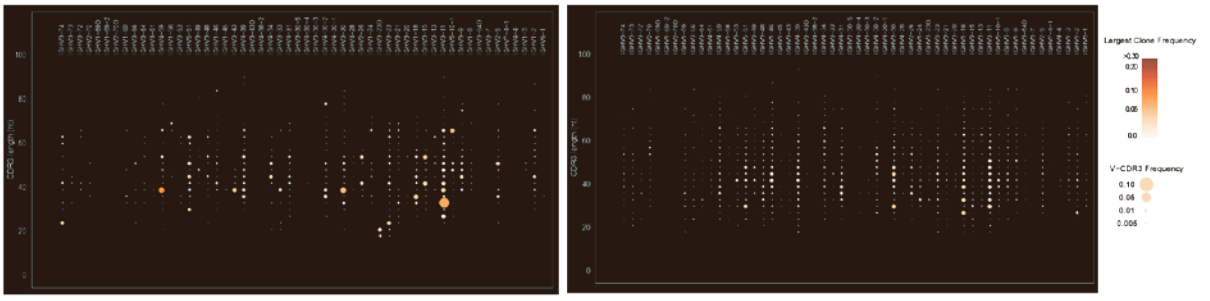

AIH Patient 2

VILI Patient 6

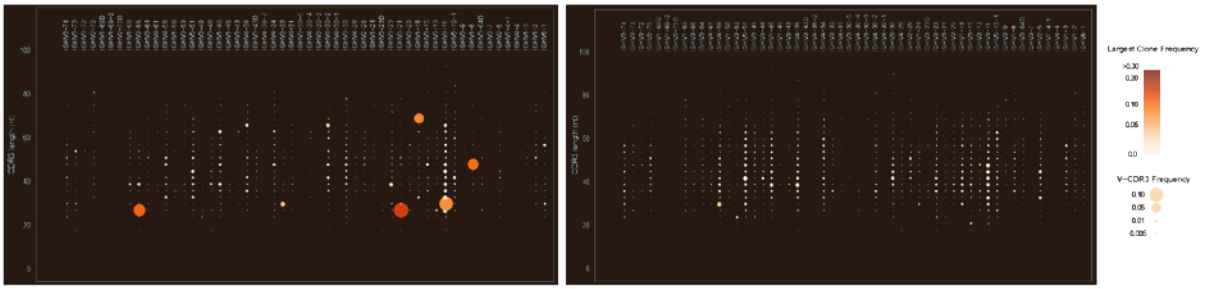

AIH Patient 3

Supp. Fig. 5. TCR and BCR Repertoire Spectratyping Plots from Two VILI and AIH Patients

(A) TCR repertoire spectratyping plots of two VILI (#2, #6) and two AIH (#2, #3) patients. The x-axis shows different TCR-β chain V genes and the y-axis shows different CDR3 nucleotide lengths. **(B)** BCR repertoire spectratyping plots of two VILI (#2, #6) and two AIH (#2, #3) patients. The x-axis shows different IgH-V genes and the y-axis shows different CDR3 nucleotide lengths. Circle size indicates the frequency of a particular variable gene-CDR3 nucleotide length combination and circle color indicates the frequency of the largest clone among other clones having the same variable gene-CDR3 nucleotide length combination.

Supplementary Table 1. Comparison of clinical and morphological features of VILI and AIH patients

	VILI (n = 6)	AIH (n = 9)	*p value VILI vs AIH*
Age, median years (range)	58 (21-85)	61(49-78)	n.s. (0.76)
Gender (female), n (%)	2 (33%)	8 (89%)	
AST/ULN, mean	38.3	18.0	ns (0.08)
ALT/ULN, mean	44.1	27.7	ns (0.30)
GGT/ULN, mean	5.3	7.6	ns (0.33)
ALP/ULN,mean	1.2	1.5	ns (0.43)
R-value, mean	44.0	19.2	ns (0.11)
Bilirubin/ULN, mean	9.2	4.0	ns (0.13)
Pattern of injury			
• Hepatocytic % (n)	100% (n = 6)	88.9% (n = 8)	
• Mixed	0	11.1% (n = 1)	
• Cholestatic	0	0	
elevated ANA and/or ASMA/AAA, % (n)	67% (4)	100% (9)	
anti-SLA, anti-LKM1, or anti-LC1	0	0	
AMA	1*	0	
ANCA	0	2	
Increased IgG, n/totally measured (%)	2/5 (40%)	4/8 (50%)	
Ishak Grading, score, mean	12.2	10.3	ns (0.34)
• Piecemeal necrosis	2.3	2.9	ns (0.39)
• Focal lytic necrosis/apoptosis/inflammation	3.7	3.4	ns (0.63)
• Portal inflammation	2.3	3.1	ns (0.16)
• Confluent necrosis	3.8	1	**0.0025**
Fibrosis			
• F0	6 (100%)	5 (55.5%)	
• F1	0	4 (44.4%)	
Eosinophils portal tract (mean/HPF)	30.0	57.8	ns (0.21)
Eosinophils lobular (mean/HPF)	11.8	12.1	ns (0.96)
Simplified AIH score ≥ 6	60% (3/5)	100 % (9/9)	

Abbreviations: AAA: anti-actin antibodies, ALP: alkaline phosphatase, ALT: alanine aminotransferase, AMA: anti-mitochondrial antibody, ANA: anti-nuclear antibody, ANCA: Anti-neutrophil cytoplasm antibodies, Anti-LC1: anti-liver cytosol type 1, Anti-LKM1: anti-liver-kidney microsome 1, Anti-SLA: anti-soluble liver antigen, ASMA: anti-smooth muscle antibody, AST: aspartate aminotransferase, GGT: Gamma-glutamyltransferase, HPF: high power field. Two-group comparison: unpaired student *t*-test. ns: not significant. *not classical AMA

Supplementary Table 2. Clinical Features of VILI and AIH patients

Supplementary Table 2 can be found as a separate supplementary document.

Supplementary Table 3. Morphological Evaluation of VILI and AIH Samples

Patient ID	Time between symptoms and liver biopsy (days)	Ishak Staging (Fibrosis)	Ishak Grading Total	Ishak Grading	Interface hepatitis (0-4)	Confluent necrosis (0-6)	Focal lytic necrosis (0-4)	Degree of Portal inflammation (0-4)
VILI1	11	0	16	4+5+4+3	4	5	4	3
VILI2	2	0	3	0+0+2+1	0	0	2	1
VILI3	11	0	16	4+5+4+3	4	5	4	3
VILI4	90	0	11	1+4+4+2	1	4	4	2
VILI5	16	0	14	3+5+4+2	3	5	4	2
VILI6	77	0	13	2+4+4+3	2	4	4	3
AIH1	9	0	14	4+2+4+4	4	2	4	4
AIH2	60	1	11	3+0+4+4	3	0	4	4
AIH3	150	0	10	3+0+4+3	3	0	4	3
AIH4	30	0	14	4+2+4+4	4	2	4	4
AIH5	120	0	12	3+2+4+3	3	2	4	3
AIH6	n.a.	1	6	2+0+2+2	2	0	2	2
AIH7	90	0	6	2+0+2+2	2	0	2	2
AIH8	n.a.	1	9	2+1+4+2	2	1	4	2
AIH9	90	1	11	3+2+3+3	3	2	3	3

Supplementary Table 4. Cohort of patients with chronic hepatitis C infection, ASH or normal liver

Number Publication	Sex	Age	Metavir_Fibrosis	Metavir_Activity	AST (U/L)	ALT (U/L)	GGT (U/L)	ALP (U/L)	Bilirubin TOT umol/l,
HCV1	m	66	F4	A3	NA	NA	NA	NA	NA
HCV2	m	53	F4	A3	109	103	242	78	7
HCV3	f	62	F4	A2	76	85	45	33	21
HCV4	m	64	F4	A3	134	132	179	70	13
HCV5	m	70	F4	A2	NA	NA	NA	NA	NA
HCV6	m	67	F4	A3	93	105	83	66	22
HCV7	m	53	F4	A3	44	41	149	105	7
HCV8	f	51	F4	A3	88	82	82	62	9
HCV9	m	46	F4	A3	127	166	66	56	10
HCV10	m	64	F4	A2	106	150	96	51	12
HCV11	f	56	F4	A3	126	126	58	83	15
HCV12	m	53	F4	A3	113	122	234	118	20
HCV13	m	61	F4	A3	35	44	152	94	13
ASH1	f	65	F4	A2	55	36	65	125	21
ASH2	m	65	F4	A2	36	16	62	41	53
ASH3	m	64	F4	A1	51	38	313	192	7,7
ASH4	m	78	F4	A1	60	54	274	117	21,9
ASH5	f	64	F4	A1	37	26	293	98	30,1
ASH6	m	80	F4	A2	74	45	61	158	80,9
ASH7	m	56	F4	A1	78	47	235	168	19,2
ASH8	f	61	F4	A1	NA	NA	NA	NA	NA
ASH9	f	73	F4	A1	NA	NA	NA	NA	NA
ASH10	f	73	F4	A1	25	34	141	47	8,2
ASH11	m	69	F4	A1	42	36	173	59	13,4
ASH12	f	70	F4	A1	59	66	337	110	13,6
ASH13	f	63	F4	A1	35	29	382	213	7
ASH14	f	48	F4	A1	163	66	181	119	282
ASH15	m	50	F4	A1	580	83	119	70	111,7
ASH16	m	72	F4	A1	93	44	104	131	20,4
ASH17	f	65	F4	A2	NA	NA	NA	NA	NA
Normal1 *	f	46	F0	A0	10	6	76	111	3.4
Normal2 †	f	70	F0	A0	61	50	367	351	10.6
Normal3 †	m	74	F0	A0	42	13	511	439	17.7

***** Metastasis of a urothelial carcinoma, normal liver histology

† Metastasis of a pancreas carcinoma, normal liver histology

Abbreviations: f: female, m: male, ALP: alkaline phosphatase, ALT: alanine aminotransferase, AST: aspartate aminotransferase, GGT: Gamma-glutamyltransferase, NA: not available, TOT: total, ASH: alcoholic steatohepatitis.

Supplementary Table 5. Genes with significant differential expression between VILI and AIH cohorts after bulk RNA sequencing

gene	baseMean	log2FoldChange	lfcSE	pvalue	padj
ABCA5	543.8661421	0.7730	0.3282	0.0008	0.0473
ABI3	565.7659818	-1.0031	0.2948	0.0000	0.0102
ARG1	17209.79428	0.9776	0.3322	0.0002	0.0259
ARHGAP26	399.3413445	-0.8445	0.3090	0.0002	0.0272
ARHGAP4	543.7854154	-1.0131	0.3802	0.0002	0.0272
ATL2	1598.865463	0.5829	0.1631	0.0000	0.0102
ATP5MD	6643.073467	0.6299	0.2390	0.0005	0.0370
BTN3A3	690.6819673	-0.8072	0.2999	0.0003	0.0273
C19orf33	18862.62998	0.6973	0.2550	0.0003	0.0310
CD99	4145.558182	1.2671	0.2797	0.0000	0.0019
CSK	666.261223	-0.6731	0.2784	0.0006	0.0414
DCTN6	858.4521553	0.7393	0.2068	0.0000	0.0102
EBPL	1304.140801	0.9047	0.2980	0.0001	0.0237
EPHB4	1456.347616	0.6296	0.2070	0.0001	0.0256
FAM229B	586.6193901	0.8230	0.3386	0.0007	0.0431
FIS1	451.1944193	-0.6963	0.2542	0.0003	0.0273
GATAD2B	423.9286002	-0.5937	0.2486	0.0008	0.0453
GBP3	1294.260635	-0.9089	0.3278	0.0002	0.0272
GDA	894.3891478	0.7796	0.2877	0.0003	0.0310
H3-5	353.4044039	-0.8586	0.3814	0.0007	0.0444
HAL	1139.962025	1.2623	0.4194	0.0001	0.0237
HEBP2	3014.700053	0.8674	0.2335	0.0000	0.0102
HGD	9254.483218	0.7722	0.3184	0.0007	0.0444
HOOK1	1366.537432	0.8817	0.2500	0.0000	0.0102
IFITM2	2016.331952	0.7132	0.2403	0.0002	0.0259
INPP4A	553.5798021	-0.8775	0.2433	0.0000	0.0102
INPP5D	372.1520739	-0.8205	0.3449	0.0006	0.0399
INSIG1	4013.458116	1.1973	0.3794	0.0001	0.0227
IRF1	1693.638604	-0.8191	0.3019	0.0002	0.0272
KDM5C	530.7694426	-0.8084	0.2742	0.0001	0.0237
LCLAT1	543.3195653	0.6482	0.2276	0.0002	0.0273
LOC101060341	1003.839707	-0.8011	0.3027	0.0003	0.0294
LOC102724971	16769.75507	-1.2340	0.5823	0.0007	0.0444
MRPS22	1230.668932	0.5804	0.2083	0.0003	0.0310
NFIC	7714.168296	0.6182	0.1933	0.0001	0.0227
NOSTRIN	415.3506798	0.7809	0.2935	0.0004	0.0330
NSD3	581.4232978	-0.6190	0.2474	0.0005	0.0385
NUCB2	1335.339463	0.8192	0.2277	0.0000	0.0102
ORC4	536.7131975	0.6807	0.2410	0.0003	0.0273
OXLD1	562.7979355	0.6239	0.2558	0.0008	0.0460
PARP14	1296.769804	-0.6581	0.2267	0.0002	0.0259
PGRMC2	4957.914803	0.5999	0.2333	0.0006	0.0399
PIGP	1112.986821	0.6031	0.2109	0.0003	0.0273
PLPP1	1944.667587	0.6116	0.2354	0.0005	0.0383

POLR2J	4907.159313	0.5971	0.2204	0.0004	0.0345
PRF1	319.5159479	-1.0617	0.4514	0.0005	0.0380
PSME2	1921.837718	-0.7045	0.2340	0.0001	0.0237
RGPD_Family	937.2468403	0.6356	0.2078	0.0002	0.0259
RNF213	1170.049883	-0.7985	0.2658	0.0001	0.0237
RTL8A	1651.651326	0.8062	0.2247	0.0000	0.0102
SAA_Family	39655.04827	3.3748	0.8766	0.0000	0.0102
SAA1	18281.59568	3.1488	0.8607	0.0000	0.0102
SCML1	474.779273	0.7891	0.2690	0.0002	0.0259
SGK2	1216.511862	0.6762	0.2257	0.0002	0.0259
SLC43A3	3160.404972	0.6393	0.2405	0.0004	0.0363
STAT1	2377.08624	-0.7457	0.3277	0.0008	0.0453
STX16	956.6470281	-0.6724	0.1854	0.0000	0.0102
TAPBP	2418.783641	-0.6273	0.2170	0.0002	0.0272
TMBIM4	6890.701946	0.5847	0.1732	0.0001	0.0166
TMC8	482.6882232	-0.9717	0.3693	0.0003	0.0274
TMEM123	21566.67719	0.6470	0.2244	0.0002	0.0272
TMEM30A	2832.842693	0.5810	0.1811	0.0001	0.0227
TRIB3	688.4571657	0.8449	0.3313	0.0005	0.0380
TRIM56	1043.163351	-0.6095	0.1917	0.0001	0.0227
TSPAN31	508.5359559	0.6713	0.2326	0.0002	0.0272
TSPAN8	1083.273206	2.1683	0.4992	0.0000	0.0019
VDAC1_VDAC3	5771.330482	0.5896	0.1818	0.0001	0.0227
VPS37B	512.0670494	-1.0833	0.2549	0.0000	0.0019
VRK3	1292.114279	-0.5827	0.1526	0.0000	0.0102
YME1L1	1022.841411	0.6577	0.2260	0.0002	0.0272

Supplementary Table 6. Gene Set Enrichment Analysis of VILI and AIH cohorts after bulk RNA sequencing

Supplementary Table 6 can be found as a separate supplementary document.

Supplementary Table 7. Differential Gene Expression Analysis of VILI and AIH cohorts after spatial transcriptomics experiment

Supplementary Table 7 can be found as a separate supplementary document.

Supplementary Table 8. Gene Set Enrichment Analysis of VILI and AIH cohort after spatial transcriptomics experiment

Supplementary Table 8 can be found as a separate supplementary document.

Supplementary Table 9. Cohort of patients with DI-AILH

Patient ID	Sex	Age	Drug	AST (U/L)	ALT (U/L)	GGT (U/L)	ALP (U/L)	Bilirubin TOT (umol/l)	Auto-antibodies
DI-AILH1	f	40	Infliximab	559	957	72	237	154.7	ANA, 1:80
DI-AILH2	f	68	Infliximab	680	1167	342	172	NA	Anti-dsDNA
DI-AILH3	f	70	Atorvastatin	851	626	215	161	31.1	ANA, 1:320
DI-AILH4	f	66	Atorvastatin	35	35	556	363	6.5	ASMA, 1:640

Abbreviations: f: female, AST: aspartate aminotransferase ALT: alanine aminotransferase, GGT: Gamma-glutamyltransferase ALP: alkaline phosphatase, NA: not available, TOT: total, ANA: anti-nuclear antibody, ASMA: anti-smooth muscle antibody

Supplementary Table 10. Morphological Evaluation of DI-AILH Samples

Patient ID	Time between symptoms and liver biopsy (days)	Metavir Staging	Ishak Grading Total	Ishak Grading	Interface hepatitis (0-4)	Confluent necrosis (0-6)	Focal lytic necrosis (0-4)	Degree of Portal inflammation (0-4)
DI-AILH1	14	F0	7	2+0+2+3	2	0	2	3
DI-AILH2	5	F0	6	2+0+2+2	2	0	2	2
DI-AILH3	26	F0	10	3+1+2+4	3	1	2	4
DI-AILH4	220	F0	4	1+0+0+3	1	0	0	3

Supplementary Table 11. SARS-CoV-2 Spike Glycoprotein Epitopes with Matched CDR3 sequence

Input_sequence	Match_sequence	Score	Epitope	Antigen	Patient
ASSTGGTEAF	ASTTGGTEAF	0.9837	KLNDLCFTNVYADSFVIR	surface glycoprotein [Severe acute respiratory syndrome coronavirus 2]	VILI1
ASSSGAASYEQY	ASSAGASSYEQY	0.9744	DLPIGINITRFQTL*	surface glycoprotein [Severe acute respiratory syndrome coronavirus 2]	VILI1
ASSSGAASYEQY	ASSAGAASYEQY	0.9837	DLPIGINITRFQTL*	surface glycoprotein [Severe acute respiratory syndrome coronavirus 2]	VILI1
ASSLIGDTQY	ASSLLGDTQY	0.9808	RSVASQSIIAYTMSL**	surface glycoprotein [Severe acute respiratory syndrome coronavirus 2]	VILI3
ASSLIGDTQY	ASSLIGETQY	0.9711	QYIKWPWYI	surface glycoprotein [Severe acute respiratory syndrome coronavirus 2]	VILI3
ASSLEGSSYNEQF	ASSLDGSSYNEQF	0.9712	VQPTESIVRFPNITNLCPF	surface glycoprotein [Severe acute respiratory syndrome coronavirus 2]	VILI3
ASSFGSTDTQY	ASSFGTTDTQY	0.9776	YLQPRTFLL	surface glycoprotein [Severe acute respiratory syndrome coronavirus 2]	VILI4
ASSQGQPQH	ASSSQGQPQH	0.9701	RSVASQSIIAYTMSL**	surface glycoprotein [Severe acute respiratory syndrome coronavirus 2]	VILI5
ASALGSNQPQH	ASSLGSNQPQH	0.9831	FGEVFNATRFASVY	surface glycoprotein [Severe acute respiratory syndrome coronavirus 2]	VILI5

***** Same epitope amino acid sequence

****** Same epitope amino acid sequence

Supplementary Table 12. T-Cell Clones of VILI #5 Liver Biopsy and Blood Sample

Supplementary Table 12 can be found as a separate supplementary document.

Supplementary Table 13. T-Cell Clones of VILI_F Liver Biopsy and Blood Sample from Different Time Points

Supplementary Table 13 can be found as a separate supplementary document.

Supplementary Table 14. Review of vaccine induced liver injury cases from literature

Supplementary Table 14 can be found as a separate supplementary document.

Supplementary Table 15. qPCR Primers

Gene	Forward Primer	Reverse Primer
RNF213	5'-GACAGAACTGCAGACCACCG-3'	5'-GGTGGCTGTTTCATTCTCTGG-3'
TSPAN8	5'-GGCGACAGGTATCCTAGGAGC-3'	5'-CAATCAGCAGCTCCATTGACC-3'
GAPDH	5'-AGGTGAAGGTCGGAGTCAACG-3'	5'-TGGAAGATGGTGATGGGATTT-3'

Supplementary Table 16. Reagents used in CODEX Experiment

Product	Company	Cat.No (#)
Coverslip	Electron Microscopy Sciences	72204-01
Poly-L-Lysine Solution	Sigma-Aldrich	P8920
10X Buffer	Akoya Biosciences	7000001
Assay Reagent	Akoya Biosciences	7000002
Nuclear Stain	Akoya Biosciences	7000003
Staining Kit	Akoya Biosciences	7000008
Antibody Conjugation Kit	Akoya Biosciences	7000009
Storage Buffer	Akoya Biosciences	232107
96 well plate	Akoya Biosciences	7000006
96 well plate seal	Akoya Biosciences	7000007
Paraformaldehyde 16% Solution	Electron Microscopy Sciences	15710
Amicon Ultra-0.5 Centrifugal Filter Unit	Merck	UFC505024

Primary Antibody	Company	Cat.No (#)	Clone Number
Anti-Liver Arginase antibody EPR6672(B) - BSA and Azide free	Abcam	ab211961	EPR6672(B)
CD20-BX007 (L26)	Akoya Biosciences	PN 232175	L26
CD8-BX026 (C8/144B)	Akoya Biosciences	PN 232151	C8/144B
CD68-BX015 (KP1)	Akoya Biosciences	PN 232176	KP1
CD4-BX003 (EPR6855)	Akoya Biosciences	PN 232174	EPR6855
CD3e-BX045 (EP449E)	Akoya Biosciences	PN 240006	EP449E
CD79a (JCB117) Mouse Monoclonal Antibody	Abcam	ab239891	EP3618
Ki67-BXO47(B56)	Akoya Bioscience	PN 232179	B56
CD31-BX001 (EP3095)	Akoya Bioscience	PN 232172	EP3095
Purified anti-Cytokeratin 19 Antibody	Biolegend	628502	A53-B/A2
Purified anti-mouse/rat/human FOXP3 Antibody	Biolegend	320002	150D

Supplementary References

1. **Boettler T.**, **Csernalabics B.**, Salie H., Luxenburger H., Wischer L., Alizei E.S., et al. SARS-CoV-2 vaccination can elicit a CD8 T-cell dominant hepatitis. J Hepatol 2022.
2. **Fontana R.J.**, Seeff L.B., Andrade R.J., Björnsson E., Day C.P.,Serrano J., et al. Standardization of nomenclature and causality assessment in drug-induced liver injury: summary of a clinical research workshop. Hepatology 2010;52:730-42.
3. **Tiniakos D.G.**, Brain J.G., Bury Y.A. Role of Histopathology in Autoimmune Hepatitis. Dig Dis 2015;33 Suppl 2:53-64.
4. **Ishak K.**, Baptista A., Bianchi L., Callea F., Groote J.D., Gudat F., et al. Histological grading and staging of chronic hepatitis. J Hepatol 1995;22:696-9.
5. **Lohse A.W.**, Sebode M., Bhathal P.S., Clouston A.D., Dienes H.P., Jain D., et al. Consensus recommendations for histological criteria of autoimmune hepatitis from the International AIH Pathology Group: Results of a workshop on AIH histology hosted by the European Reference Network on Hepatological Diseases and the European Society of Pathology: Results of a workshop on AIH histology hosted by the European Reference Network on Hepatological Diseases and the European Society of Pathology. Liver Int 2022;42:1058-1069.
6. **Qu L.M.**, Wang S.H. Yang K., Brigstock D.R., Sun L., Gao R. et al. CD4(+)Foxp3(+)CD25(+/-) Tregs characterize liver tissue specimens of patients suffering from drug-induced autoimmune hepatitis: A clinical-pathological study. Hepatobiliary Pancreat Dis Int 2018;17:133-139.
7. **Love M.I.**, Huber W., Anders S. Moderated estimation of fold change and dispersion for RNA-seq data with DESeq2. Genome Biol 2014;15:550.
8. **Zhu A.**, Ibrahim J.G., Love M.I. Heavy-tailed prior distributions for sequence count data: removing the noise and preserving large differences. Bioinformatics 2019;35:2084-2092.
9. **Livak K.J.**, Schmittgen T.D. Analysis of relative gene expression data using real-time quantitative PCR and the 2(-Delta Delta C(T)) Method. Methods 2001;25:402-8.
10. **Merritt C.R.**, Ong G.T., Church S.E., Barker K., Danaher P., Geiss G., et al. Multiplex digital spatial profiling of proteins and RNA in fixed tissue. Nat Biotechnol 2020;38:586-599.
11. **Casarrubios M.**, **Cruz-Bermudez A.**, Nadal E., Insa A., Campelo M.D.R.G, Lazaro M., et al. Pretreatment Tissue TCR Repertoire Evenness Is Associated with Complete Pathologic Response in Patients with NSCLC Receiving Neoadjuvant Chemoimmunotherapy. Clin Cancer Res 2021;27:5878-5890.

12. **Zhang J.**, **Ji Z.**, **Caushi J.X.**, **Asmar M.E.**, Anagnostou V., Cottrell T.R., et al. Compartmental Analysis of T-cell Clonal Dynamics as a Function of Pathologic Response to Neoadjuvant PD-1 Blockade in Resectable Non-Small Cell Lung Cancer. Clin Cancer Res 2020;26:1327-1337.
13. Van der Loo M. The stringdist package for approximate string matching. The R Journal, 6, 111-122, https://CRAN.R-project.org/package=stringdist 2014.
14. Wickham H. ggplot2: Elegant Graphics for Data Analysis. Springer-Verlag New York. ISBN 978-3-319-24277-4. https://ggplot2.tidyverse.org 2016.
15. **Schindelin J.**, Arganda-Carreras I., Frise E., Kaynig V., Longair M., Pietzsch T., et al. Fiji: an open-source platform for biological-image analysis. Nat Methods 2012;9:676-82.
16. **Thevenaz P.**, Ruttimann U.E., Unser M. A pyramid approach to subpixel registration based on intensity. IEEE Trans Image Process 1998;7:27-41.
17. **Preibisch S.**, Saalfeld S., Tomancak P. Globally optimal stitching of tiled 3D microscopic image acquisitions. Bioinformatics 2009;25:1463-5.
18. **Guiet R.**, Burri O., Chiaruttini N., Seitz A., Eglinger J. Kheops (Version 0.1.8) [Computer software]. https://doi.org/10.5281/zenodo.5256256 2021.
19. **Bankhead P.**, Loughrey M.B., Fernández J.A., Dombrowski Y., McArt D.G., Dunne P.D., et al. QuPath: Open source software for digital pathology image analysis. Scientific Reports 2017;7:16878.
20. **Uhlen M.**, Fagerberg L., Hallstrom B.M., Lindskog C., Oksvold P., Mrdinoglu A., et al. Proteomics. Tissue-based map of the human proteome. Science 2015;347:1260419.
21. **Schmidt U.**, Weigert M., Broaddus C., Myers G. (2018). Cell Detection with Star-Convex Polygons. MICCAI 2018. Lecture Notes in Computer Science, vol 11071. Springer, Cham. 2018.
22. **Levine J.H.**, **Simonds E.F.**, **Bendall S.C.**, Davis K.L., Amir E.D., Tadmor M.D., et al. Data-Driven Phenotypic Dissection of AML Reveals Progenitor-like Cells that Correlate with Prognosis. Cell 2015;162:184-97.